ARO 15407.9-EL

LEVEL II

(11)

AD A093810

STUDIES OF A CLASS OF
LOW-PROFILE ANTENNAS

Liang C. Shen and Stuart A. Long

U. S. Army Research Office
Grant DAAG 29-78-G-0198
Contract DAAG 29-79-C-0202

December 1980

DTIC

JAN 1 2 1981

C

UNIVERSITY OF HOUSTON

Founded 1927

DDC FILE COPY

Department of Electrical Engineering

Cullen College of Engineering

University of Houston

Studies of a Class of Low-Profile Antennas

Final Report

Liang C. Shen

Stuart A. Long

November 1980

U. S. Army Research Office

DAAG 29-78-G-0198
DAAG 29-79-C-0202

Department of Electrical Engineering
University of Houston
Houston, Texas   77004

Approved for Public Release
Distribution Unlimited

81 1   12 086

SECURITY CLASSIFICATION OF THIS PAGE *(When Data Entered)*

REPORT DOCUMENTATION PAGE		READ INSTRUCTIONS BEFORE COMPLETING FORM
1. REPORT NUMBER	**2. GOVT ACCESSION NO.** AD·AC93 810	**3. RECIPIENT'S CATALOG NUMBER**
4. TITLE *(and Subtitle)* Studies of a Class of Low-Profile Antennas		**5. TYPE OF REPORT & PERIOD COVERED** Final Report Sept. 20, 1978–Sept. 19,1980
		6. PERFORMING ORG. REPORT NUMBER
7. AUTHOR(s) Liang C. Shen and Stuart A. Long		**8. CONTRACT OR GRANT NUMBER(s)** DAAG 29-78-G-0198 DAAG 29-79-C-0202
9. PERFORMING ORGANIZATION NAME AND ADDRESS Department of Electrical Engineering University of Houston Houston, Texas 77004		**10. PROGRAM ELEMENT PROJECT, TASK AREA & WORK UNIT NUMBERS**
11. CONTROLLING OFFICE NAME AND ADDRESS U. S. Army Research Office Post Office Box 12211 Research Triangle Park, NC 27709		**12. REPORT DATE** December, 1980
		13. NUMBER OF PAGES
14. MONITORING AGENCY NAME & ADDRESS*(If different from Controlling Office)*		**15. SECURITY CLASS. *(of this report)*** Unclassified
		15a. DECLASSIFICATION/DOWNGRADING SCHEDULE NA

16. DISTRIBUTION STATEMENT *(of this Report)*

Approved for public release; distribution unlimited.

17. DISTRIBUTION STATEMENT *(of the abstract entered in Block 20, If different from Report)*

NA

18. SUPPLEMENTARY NOTES

19. KEY WORDS *(Continue on reverse side if necessary and identify by block number)*

printed-circuit antenna; microstrip antenna; circular disc antenna;
elliptical antenna; circularly polarized antenna.

20. ABSTRACT *(Continue on reverse side if necessary and identify by block number)*

Circular and elliptical printed-circuit antennas have been investigated
both experimentally and theoretically. A more rigorous analysis incorporating
a surface admittance boundary condition has been developed. The elliptical
antenna has been shown to provide circular polarization for a proper choice
of feed location and eccentricity of the ellipse.

DD FORM 1473 EDITION OF 1 NOV 65 IS OBSOLETE

THE FINDINGS IN THIS REPORT ARE NOT TO BE
CONSTRUED AS AN OFFICIAL DEPARTMENT OF
THE ARMY POSITION, UNLESS SO DESIGNATED
BY OTHER AUTHORIZED DOCUMENTS.

Accession For

NTIS CRA&I
DTIC TAB ☐
Unannounced ☐
Justification

By
Distribution/

Availability Codes

Dist | Avail and/or
      | Special

A

TABLE OF CONTENTS

STATEMENT OF PROBLEM

Printed-circuit or microstrip antennas have proven to be extremely useful in a wide variety of applications requiring radiators that are both low-profile and conformal. Previous theoretical investigations have relied on simple models, which provide very useful information, but are limited in their applicability and accuracy. During the present project a more rigorous theoretical approach has been developed. In addition a radiator with a new geometrical shape, that of an ellipse, has been investigated both theoretically and experimentally. The resulting antenna is able to provide circular polarization using only a single simple feed network.

1

SUMMARY OF RESULTS

Several problems associated with low-profile antennas were addressed in this project. A large portion of the effort was directed toward printed-circuit or microstrip, type antennas.

From the time of their inception printed-circuit antennas have been plagued by a seemingly insurmountable problem of excessively small bandwidth. From all indications there seems to be little one can do to improve the bandwidth beyond simply increasing the thickness of the substrate. This method cannot, however, be extended too far without the loss of the highly desirable low-profile characteristic of the antenna. In some applications increased bandwidth is only needed so the antenna can operate at two distinct frequencies which may be too far apart for one antenna to operate efficiently at both frequencies. For this purpose a dual frequency antenna was designed by stacking two slightly different sized circular discs. Through a proper choice of the two disc diameters and their spacings, the two resonant frequencies can be adjusted to the desired values. The technical details have been previously published and are included in Appendix A.

Early analysis techniques for printed-circuit type antennas treated the antenna as a resonant cavity bounded above and below by conducting plates and on its sides by perfectly conducting magnetic walls. This assumption limits the model to very thin dielectric substrates and results in an infinite input impedance at resonance. During this project the antenna was modeled as a cavity with a finite admittance wall on its side surfaces. This admittance surface was

2

determined by the radiated power and fringing field at the edge of the radiator. Using this improved model the input impedance can be calculated directly and results in better agreement with previous experimental data. The technical details and specific comparisons with experimental results have been published and are shown in Appendices B and C.

In its usual simple configuration whether rectangular or circular, the printed-circuit antenna produces a linearly polarized radiation pattern. In many applications, however, circular polarization is required. Through the use of multiple feeds and phase shifters circular polarization can be provided, but with the obvious increase in the complexity of the total radiating structure. In an attempt to solve this problem, the elliptical printed-circuit antenna was investigated theoretically. The results show that circular polarization can be provided with a single, simple feed by simply making the shape of the radiator slightly elliptical.

The boundary value problem to be solved consisted of an elliptical cavity surrounded by a surface admittance wall as previously derived for the circular disc case. Standard elliptical coordinates can be used and the resulting fields expressed in terms of Mathieu functions. To provide circular polarization the ellipse must have a very small eccentricity and is, therefore, almost circular. For these small eccentricities approximate formulas are available for Mathieu functions in terms of more frequently tabulated Bessel functions. Using these calculated interior fields the total radiated fields can then be determined. For a proper choice of eccentricity good circular polar-

3

ization is predicted for a feed located along a radius at a 45° angle from the major axis of the ellipse. The opposite handedness polarization can be generated by placing the feed at -45° from the major axis. The detailed theoretical derivation has been accepted for publication and is included in Appendix D.

A systematic experimental investigation was also undertaken to study the elliptical printed-circuit antenna. Several sets of ellipses were etched on printed circuit boards of varying thicknesses. The slightly elliptical discs varied from a minor to major axis ratio of 1.0 (that of a circle) to 0.96. The field patterns were measured for each disc at several frequencies near the frequency where best circular polarization was obtained. In addition the axial ratio was measured for each antenna as a function of frequency. Finally, the input impedance of each radiator was measured. The data was compared to available theoretical predictions and overall agreement was found. Detailed measurements are illustrated in a paper accepted for publication that is included in Appendix E.

Participating Scientific Personnel

Dr. Liang C. Shen, Principal Investigator

Dr. Stuart A. Long, Co-principal Investigator

Brij Popli, Master of Science in Electrical Engineering

Jai-Dong Ou, Graduate Studnet, Degree in Progress

Mark W. McAllister, Graduate Student, Degree in Progress

Shabbir Chowdhury, Graduate Student, Degree in Progress

List of Publications

Stuart A. Long and M. D. Walton, "A Dual Frequency, Stacked Circular Disc Antenna," IEEE Trans. Antennas and Propagation, Vol. AP-27, pp. 270-273, March 1979.

Liang C. Shen, "Analysis of a Circular-Disc Printed-Circuit Antenna, Proc. IEE, Vol. 126, No. 12, Dec. 1979, pp. 1220-1222.

W. C. Chew, J. A. Kong, and Liang C. Shen, "Radiation Characteristics of a Circular Microstrip Antenna," J. Appl. Phys., Vol. 51, July 1980, pp. 3907-3915.

Liang C. Shen, "The Elliptical Microstrip Antenna with Circular Polarization," IEEE Trans. Antennas and Propagation, Vol. AP-29, Jan. 1981.

Stuart A. Long, Liang C. Shen, Daniel H. Schaubert, and Frederick G. Farrar, "An Experimental Study of the Circular-Polarized, Elliptical, Printed-Circuit Antenna," IEEE Trans. Antennas and Propagation, Vol. AP-29, Jan. 1981.

List of Presentations

Stuart A. Long and M. D. Walton, "A Dual Frequency, Stacked Circular Disc Antenna," paper presented at the IEEE/AP-S International Symposium, University of Maryland, College Park, Maryland, May 1978.

Stuart A. Long and L. C. Shen, "Theoretical and Experimental Study of the Circular Printed-Circuit Antenna," paper presented at the 48th Interservice Antenna Group Meeting, Pacific Missile Test Center, Point Mugu, Ca., February 1979.

L. C. Shen and Stuart A. Long, "Theoretical Analysis of Printed Circuit Antennas," invited paper presented at the Printed Circuit Antenna Technology Workshop, Army Research Office and Physical Science Laboratory, Las Cruces, N. M., October 1979.

Stuart A. Long, "Experimental and Theoretical Studies of Printed-Circuit Antennas," Electrical Engineering Department Seminar, University of Mississippi, April, 1980.

Stuart A. Long and L. C. Shen, "The Circularly Polarized Elliptical Printed-Circuit Antenna," paper presented at the IEEE/AP-S International Symposium, Quebec, Canada, June, 1980.

A Dual-Frequency Stacked Circular-Disc Antenna

STUART A. LONG, MEMBER, IEEE, AND
MARK D. WALTON

Abstract The dual-frequency behavior of a pair of stacked circular-disc printed-circuit antennas is investigated experimentally. The input impedance is measured as a function of the sizes of the discs with emphasis placed on the values of the two resultant resonant frequencies.

I. INTRODUCTION

In recent years the use and interest in printed-circuit (or microstrip) antennas has become widespread. A wide variety of shapes and configurations have been developed into useful radiating systems. In addition to being low profile, their positive attributes include ruggedness, ease of construction, and low cost. Perhaps the sole major problem of the entire class of antennas is their seemingly inherent narrow bandwidth. Little progress has been reported in overcoming this major obstacle. The most usual method of increasing the bandwidth is simply to increase the thickness of the dielectric between the radiator and the ground plane. This method cannot, however, be extended too far without the loss of the highly desirable low-profile characteristics of the antenna. Such a technique results in only minimal increases in the bandwidth with the resulting thicker antenna still being quite narrow-band in the usual sense (less than 2 percent). Some significant increases in bandwidth have been reported for a more complicated feed arrangement using two probes and a balun [1].

For some uses, however, the increased bandwidth is actually needed for only two distinct frequencies which may be too far apart for a single antenna to operate efficiently at both frequencies. The behavior of the antenna characteristics for the range of intermediate frequencies may be of little or no
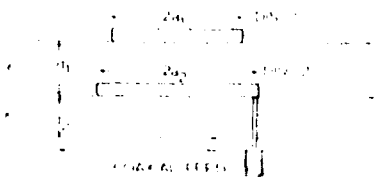
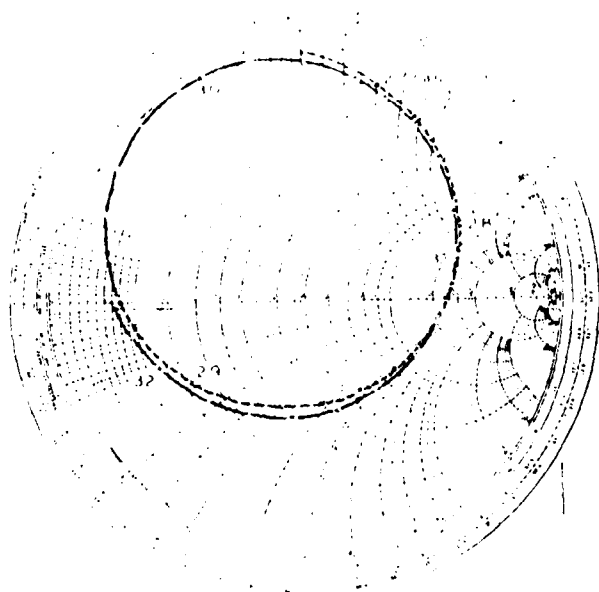Fig. 1   Stacked circular-disc antenna structure

Fig. 2   Smith chart impedance of stacked structure.

concern. For this purpose a dual-frequency antenna can be de-signed by stacking two slightly different sized circular discs. Through a proper choice of the two disc diameters and their spacings, two separate resonances can be found and adjusted to the desired values [2].

II. EXPERIMENTAL MEASUREMENTS

The proper feeding method is not necessarily apparent for the stacked circular-disc structure. To provide the desired dual-frequency behavior the inner conductor of the coaxial feed is allowed to pass through a clearance hole in the lower disc and is then electrically connected to the upper disc, as shown in Fig. 1. The actual antenna measured consisted of two circular discs which were photoetched on separate microwave printed-circuit boards and then carefully aligned so that their centers were along the same line perpendicular to the ground plane. The driving-point impedance was then measured as a function of frequency using a network analyzer for the stacked struc-ture. The sizes of the two discs and their respective spacings could be varied and the resulting behavior of the antenna char-acteristics then noted.

The majority of the measurements were carried out for a structure with the lower-disc diameter $2a_2 = 3.78$ cm and with the two spacings $d_1 = d_2 = 0.075$ cm (approximately 1/32 in each). The dielectric material was teflon-fiberglass with a rela-tive permittivity of $\epsilon_r = 2.47$. The upper-disc diameter $2a_1$ vas then varied in several increments from 3.5–4.0 cm with the feed position located near a point one-half the radius from the center of the disc.

A typical impedance, that for $2a_1 = 3.78$ cm (the same size as the lower disc), is shown in the Smith chart of Fig. 2. In-
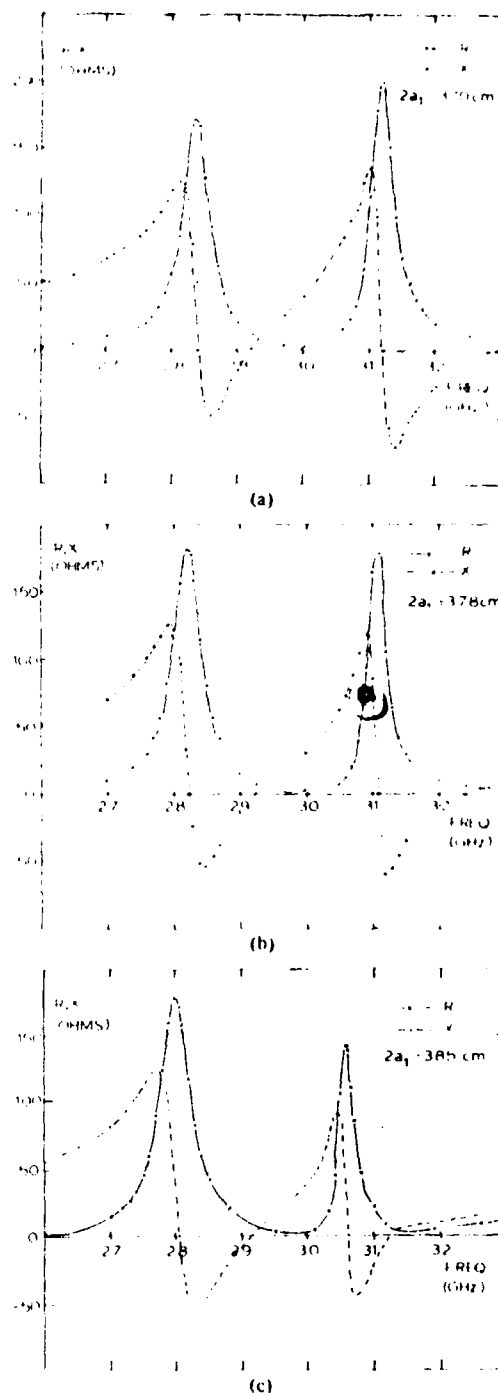

Fig. 3.   Real and imaginary parts of impedance of stacked structure.
(a) $2a_1 = 3.70$ cm. (b) $2a_1 = 3.78$ cm. (c) $2a_1 = 3.85$ cm.

stead of the usual circle that would be measured for a single circular-disc printed-circuit antenna, two very distinct circles are seen. Each of these circles crossing the right-hand real axis corresponds to one of the two desired resonances. Plots of the real and imaginary parts of the impedance versus frequency il-lustrate this dual-frequency behavior more clearly. Three typi-cal cases corresponding to values of $2a_1 = 3.70, 3.78,$ and 3.85 cm are shown in Fig. 3. Separations of 10 percent between the two resonances are clearly evident. This is far too wide a separ-ation to be covered by a single disc with a simple coaxial feed.
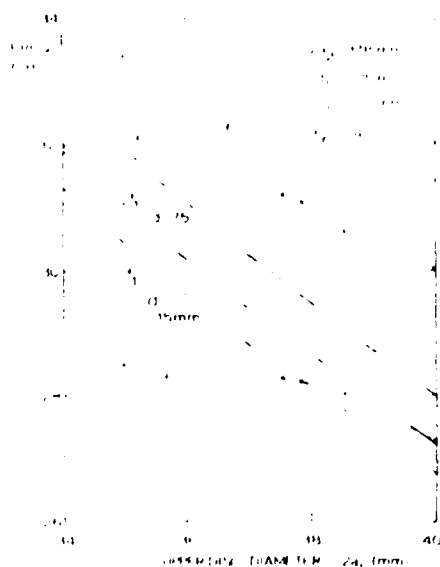
Fig. 4.   Resonant frequencies versus upper-disc diameter.

TABLE I
RESONANT FREQUENCIES AND MAXIMUM RESISTANCES FOR
STACKED CIRCULAR DISC ANTENNAS

$2a_1$ (cm)	$2a_2$ (cm)	d_1 (cm)	d_2 (cm)	f_L (GHz)	R_L (ohms)	f_U (GHz)	R_U (ohms)
3.50	3.78	.075	.075	2.853	157	3.338	189
3.70	3.78	.075	.075	2.840	167	3.120	200
3.75	3.78	.075	.075	2.830	175	3.120	185
3.78	3.78	.075	.075	2.825	182	3.110	177
3.80	3.78	.075	.075	2.820	179	3.123	182
3.85	3.78	.075	.075	2.804	178	3.060	142
4.00	3.78	.075	.075	2.728	175	3.009	97
3.78	3.78	.0135	.075	2.863	154	3.732	97
4.00	3.78	.075	.0363	2.810	95	3.250	75

Fig. 5.   Radiation patterns of stacked circular-disc antenna. (a) f = 2.83 GHz. (b) f = 3.1 GHz. (c) f = 2.9 GHz.

The functional behavior of these resonant frequencies can be investigated for varying sizes of the upper disc. The two dashed curves in Fig. 4 show the upper (f_U) and lower (f_L) resonant frequencies as the diameter of the upper disc is varied. For comparison, the theoretical zeroth-order resonant frequency (f_0) for a single disc of diameter $2a_1$ is also shown in Fig. 4. In addition, the theoretical first-order resonant frequency (f_1) which takes into account the effect of the finite-size thickness of the dielectric [3] is also shown as a function of its diameter for two thicknesses, d_1 and $d_1 + d_2$. The lower resonance (f_L) is relatively constant, remaining near the value of a single disc with $2a = 3.78$ cm and $d = .075$ cm. The upper resonance (f_U) is highly dependent on the size of the upper disc with a functional behavior similar to a single, but slightly larger, disc. A summary of the data taken, including those cases shown in Fig. 3, is presented in tabular form in Table I.

It is thus possible to effectively set the approximate value of f_L by the choice of the size of the lower disc, and then, relatively independently set f_U by a proper choice of the upper-disc diameter. Variations in the positions of the reso-
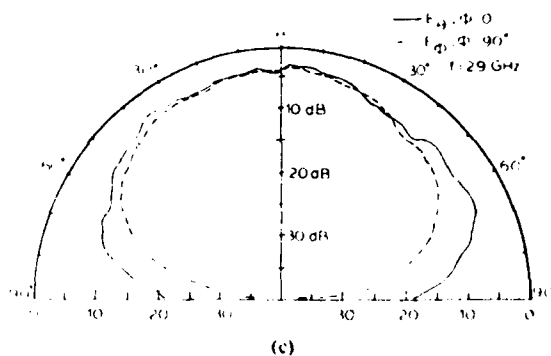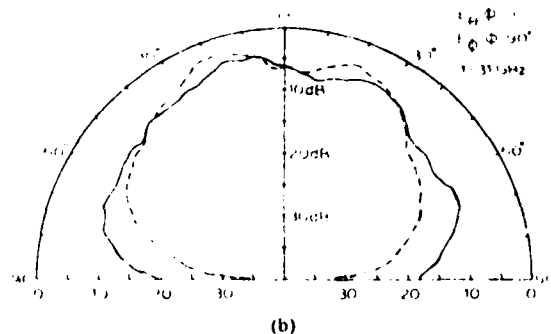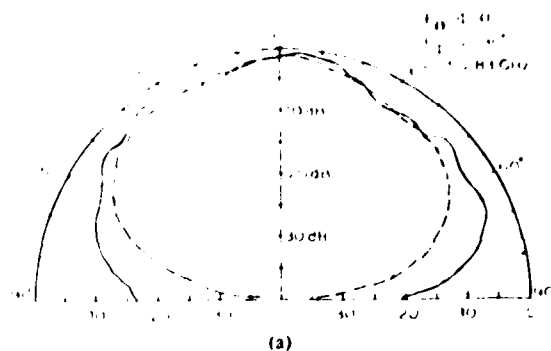
nances also result when d_1 and d_2 are changed. A limited set of data for this case is included in Table I for reference.

The far-field radiation patterns were measured in an anechoic chamber near the measured resonant frequencies for the particular structure with $2a_1 = 2a_2 = 3.78$ cm and $d_1 = d_2 = 0.075$ cm. The results are shown in Fig. 5 for each of the resonant frequencies and for one intermediate frequency. In each case the fields in the two principal planes are shown, first E_θ for $\phi = 0°$ (E-plane) and then E_ϕ for $\phi = 90°$ (H-plane). (The feed is located at $\phi = 0$.) At $f_L = 2.83$ GHz the fields are seen to be almost exactly the same as those of a single disc [4]. In each plane a rather broad pattern is found with the value of E_θ still finite in the $\theta = 90°$ plane but with a natural null for E_ϕ there. At $f_U = 3.1$ GHz the basic pattern is still the same, but some pattern deterioration has begun to show in the form of a small dip at broadside. An additional measurement at $f = 2.9$ GHz shows that the pattern is still very well formed, but there would be a very sizable impedance mismatch at this frequency. It is therefore seen that the narrow bandwidth is primarily due to the impedance variation and not due to pattern deterioration.
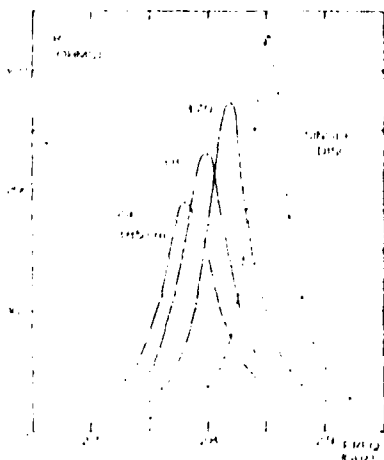
Fig. 6.   Real part of impedance with lower disc driven.

III. STACKED STRUCTURE WITH LOWER DISC DRIVEN

Connecting the feed directly to the lower disc and allowing the upper one to be purely parasitic produces an entirely different impedance behavior. When plotted on a Smith chart the impedance forms only one circle in the same fashion as a single disc. For this radiator the inclusion of the upper disc affects both the resonant frequency and the maximum value of the resistance. This behavior is seen in Fig. 6 where the real part of the impedance is plotted versus frequency for several different sizes of upper discs. Each are edge driven with $2a_2 = 3.78$ cm, $d_1 = d_2 = 0.075$ cm, and the particular upper-disc diameter as shown. The inclusion of larger discs is seen to shift the resonant frequency down in value and also to decrease the value of the maximum resistance. Some slight improvement in bandwidth is also seen from the relatively broader resonance curves.

IV. CONCLUSION

When additional bandwidth is only needed at two discrete frequencies the stacked circular-disc antenna can be useful. Even though the bandwidth around each resonant frequency is only about 1 percent, two frequencies separated by 10 percent or more can be accommodated. A proper feeding structure is, however, extremely important to insure the desired dual-frequency behavior.

REFERENCES

[1] F. V. Byron, "Antenna design for Project Camel," Hughes Aircraft Company and Applied Physics Laboratory, Tech. Memo. TG 1101, Feb. 1970.

[2] G. G. Sanford, "Multiple resonance radio frequency microstrip antenna structure," U.S. Patent 4 070 676, Jan. 1978.

[3] I. C. Shen, S. A. Long, M. R. Allerding, and M. D. Walton, "Resonant frequency of a circular disc, printed circuit antenna," IEEE Trans. Antennas Propagat., vol. AP-25, pp. 595–596, July 1977.

[4] M. D. Walton, S. A. Long, and L. C. Shen, "An experimental measurement of the radiation fields and the Q-factor of a circular disc antenna," Electromagnet. Lab., Dep. Elec. Eng., Univ. Houston, Houston, TX, Tech. Rep. TR-77-02, Oct. 1977.

Analysis of a circular-disc printed-circuit antenna

Liang C. Shen, Ph.D.

Abstract

The input impedance and the electromagnetic fields of a circular-disc printed-circuit antenna are found. The antenna is driven at an arbitrary point. The present analysis takes into account the radiation through the side wall and the fringe field at the edge of the printed-circuit antenna.

1 Introduction

Printed-circuit antennas operating at microwave frequencies are now commonly used on many flying objects and satellites. Fig. 1 shows a simple circular-disc antenna etched on a microwave printed-circuit board. The antenna has a radius equal to a, and is driven by a coaxial line through the ground plane at radial distance b from the centre. The thickness and the dielectric constant of the substrate of the printed-circuit board are denoted d and ϵ_1, respectively. The permeability μ of the substrate is equal to that of the air, i.e. $\mu = \mu_0$.

In previous studies,[1] analytical formulas for the electromagnetic fields inside the antenna are derived by treating the antenna as a resonant cavity bounded above and below by conducting plates and on the side by a perfect magnetic wall. It has been shown that, from this simple model of the antenna, the radiated fields can be obtained in simple analytic forms which agree quite well with the measured data. However, this simple model will lead to infinite input impedance and infinite electromagnetic fields at the resonant frequency.[2] This difficulty is avoided in previous work by using equivalent circuits.[3,4] The limitation of this approach is that the dielectric substrate must be very thin.
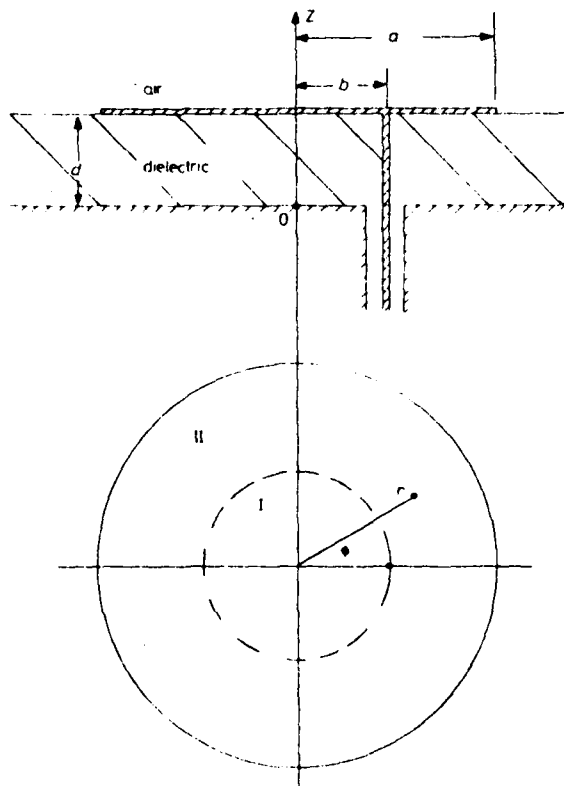

Fig. 1
Circular-disc printed-circuit antenna with coaxial feed at $r = b$.

In the present analysis, the antenna is modelled as a cavity with finite admittance wall on its side surface. The admittance surface is determined by the radiated power and fringe field on the edge of the antenna. Using this model, the input impedance can be calculated directly from the basic definition.

2 Fields inside model cavity

Assume that $k_1 d \ll 1$ where $k_1 = \omega\sqrt{\mu\epsilon_1}$, ω being the angular frequency, so that fields do not vary in the z direction. The total fields due to a constant current I_0 maintained by the coaxial line at $r = b$ are given as follows.

In region I,

$$E_z = \sum_{n=0}^{\infty} A_n J_n(k_1 r) \cos n\phi \tag{1a}$$

$$H_r = \frac{1}{\omega\mu r} \sum_{n=0}^{\infty} n A_n J_n(k_1 r) \sin n\phi \tag{1b}$$

$$H_\phi = \frac{jk_1}{\omega\mu} \sum_{n=0}^{\infty} A_n J_n'(k_1 r) \cos n\phi \tag{1c}$$

and, in region II,

$$E_z = \sum_{n=0}^{\infty} [B_n J_n(k_1 r) + C_n Y_n(k_1 r)] \cos n\phi \tag{2a}$$

$$H_r = \frac{1}{\omega\mu r} \sum_{n=0}^{\infty} n[B_n J_n(k_1 r) + C_n Y_n(k_1 r)] \sin n\phi \tag{2b}$$

$$H_\phi = \frac{jk_1}{\omega\mu} \sum_{n=0}^{\infty} [B_n J_n'(k_1 r) + C_n Y_n'(k_1 r)] \cos n\phi \tag{2c}$$

where J_n, Y_n, J_n' and Y_n' are Bessel functions of the first and the second kind, and their derivatives, respectively. A_n, B_n and C_n are constants to be determined later. The time factor $e^{j\omega t}$ is assumed throughout the analysis.

The following boundary conditions are then imposed:

$$H_{\phi n} = y_{sn} E_{zn} \qquad (\text{at } r = a) \tag{3a}$$

$$E_{z1} = E_{z2} \text{ or } H_{r1} = H_{r2} \qquad (\text{at } r = b) \tag{3b}$$

$$H_{\phi 2} - H_{\phi 1} = (I_0/b)\delta(\phi) \qquad (\text{at } r = b) \tag{3c}$$

Note that the boundary condition, eqn. 3a, is equivalent to stating that the cavity is bounded at $r = a$ by an admittance surface y_{sn}. The value of y_{sn} will be determined later.

The constants A_n, B_n and C_n in eqns. 1 and 2 are solved to satisfy eqn. 3, with the following result:

$$A_n = \frac{jI_0\omega\mu}{2(1 + \delta_n)} \frac{1}{D_n} \{J_n(k_1 b)[Y_n'(k_1 a) + j\xi_1 y_{sn} Y_n(k_1 a)]$$
$$- D_n Y_n(k_1 b)\} \tag{4a}$$

$$B_n = \frac{jI_0\omega\mu}{2(1 + \delta_n)} \frac{1}{D_n} J_n(k_1 b)[Y_n'(k_1 a) + j\xi_1 y_{sn} Y_n(k_1 a)] \tag{4b}$$

$$C_n = \frac{+jI_0\omega\mu}{2(1 + \delta_n)} J_n(k_1 b) \tag{4c}$$

where δ_n is zero for $n > 0$ and is equal to 1 for $n = 0$. $\xi_1 = (\mu/\epsilon_1)^{1/2}$. Also,

$$D_n = J_n'(k_1 a) + j\xi_1 y_{sn} J_n(k_1 a) \tag{5}$$

Note that, when $k_1 a$ is equal to one of the zeros of $J_n'(x)$ and when y_{sn} is neglected, D_n will vanish and A_n and B_n will become infinite.

3 Radiated fields

The radiated fields may be calculated from the aperture field at $r = a$. For the index n (called the nth mode) the following formulas are derived for the radiated fields:

$$E_{\theta n} = -E_n a j^n \frac{e^{-jk_0 r}}{r} \frac{\sin(k_0 d \cos\theta)}{\cos\theta} J_n'(k_0 a \sin\theta) \cos n\phi \tag{6a}$$

$$E^r_{\phi n} = E_n n j^{n} \frac{c}{r} \cdots \frac{\sin(k_0 d \cos\theta)}{k_0 \sin\theta} J_n(k_0 a \sin\theta) \sin n\phi \quad (6b)$$

where

$$F_n = B_n J_n(k_1 a) + C_n Y_n(k_1 a) \text{ and } k_0 = \omega(\mu\epsilon_0)^{1/2}$$

4 Surface admittance

The surface admittance y_{sn} associated with the nth mode is defined in eqn. 3a. The real part of $y_{sn} = g_{sn} + j b_{sn}$ is related to the total radiated power P_{rad} as follows.

$$g_{sn} = \frac{P_{rad}}{\frac{1}{2}\iint |E_z|^2 ds} \quad (7)$$

where the integration is over the cylindrical surface at $r = a$ bounded by $0 \leqslant z \leqslant d$. The radiated power may be obtained by integrating the Poynting vector over a large hemisphere using eqn. 6. The result is as follows

$$g_{sn} = \frac{d}{2a(1+\delta_n)\zeta_0}[(1+\delta_n)(k_0 a)^2 I_1 + n^2(1-\delta_n)I_2] \quad (8)$$

where $\zeta_0 = (\mu/\epsilon_0)^{1/2}$.

$$I_1 = \int_0^\pi [J_n'(k_0 a \sin\theta)]^2 \sin\theta d\theta \quad (9a)$$

and

$$I_2 = \int_0^\pi \frac{\cos^2\theta}{\sin\theta} [J_n(k_0 a \sin\theta)]^2 d\theta \quad (9b)$$

In the above formulas, $k_0 d$ has been taken to be much less than unity so that in eqn. 6 $\sin(k_0 d \cos\theta)$ is approximated by $(k_0 d \cos\theta)$.

The imaginary part of y_{sn} is mainly due to the fringe field. To estimate it, let eqn. 5 be written in terms of real and imaginary parts.

$$D_n = [J_n'(k_1 a) - \zeta_1 b_{sn} J_n(k_1 a)] + j\zeta_1 g_{sn} J_n(k_1 a) \quad (10)$$

In the zeroth-order theory, the radiation is neglected; hence $g_{sn} = 0$. The fringe field is also neglected resulting in $b_{sn} = 0$. The resonant frequency is then determined simply by the j_{ns}', the sth zero of J_n'. In a recent paper,[5] the effect of the fringe field is taken into account. It is shown that the effect of the fringe field is to lower the resonant frequency by a factor equal to $(1 + \Delta)^{1/2}$, where

$$\Delta = \frac{2d\epsilon_0}{\pi\epsilon_1 a}\left|\ln\left(\frac{\pi a}{2d}\right) + 1.7726\right|$$

Thus the model cavity will be resonant when

$$k_1 a = j_{ns}'/(1+\Delta)^{1/2} \quad (11)$$

Using this result, it is clear that D_n should vanish when $g_{sn} = 0$ and $k_1 a$ satisfies eqn. 11. In other words,

$$b_{sn} = J_n'(w)/[\zeta_1 J_n(w)] \quad (12)$$

with $w = j_{ns}'/(1+\Delta)^{1/2}$.

This completes the derivation of the formulas for the internal and the radiated fields.

5 Internal electromagnetic fields

In practice a circular-disc printed-circuit antenna is operating near the resonance of the $n = 1$ mode since it yields a strong radiation in the z-direction. In the design of such an antenna, electromagnetic fields are assumed to be zero for all other modes. The present theory enables us to check the validity of this assumption. For example, consider a printed-circuit antenna of moderate thickness with $d = 0.16$ cm, $a = 1.88$ cm, $\epsilon_1 = 2.47\epsilon_0$ and $b = 0.94$ cm. From eqn. 11, the resonant frequency for $n = 1$ mode is 2.833 GHz. Fig. 2(i) shows a plot of $|E_z|$ as a function of r for the first 11 modes in the antenna at this resonant frequency. The fields are obtained from eqns. 1, 2 and 4, with y_{sn} set equal to zero for all n except $n = 1$. The value y_{s1} is calculated from eqns. 8 and 12. It is noted that in Fig. 2(i) the field at the edge for the $n = 1$ mode is at least 37 dB higher than that of any other mode. Thus, it is a good approximation to neglect y_{sn} for all other modes except that of the $n = 1$ mode. Figs. 2(ii) and 2(iii) show the fields in the antenna at frequencies considerably lower than the resonant frequency. The $n = 1$ mode is still dominant in the cavity at these frequencies.

6 Input impedance

The input impedance is defined as[6]

$$Z_{in} = \frac{j 4 I_i}{P_i + 2j\omega(W_e - W_m)} \quad (13)$$
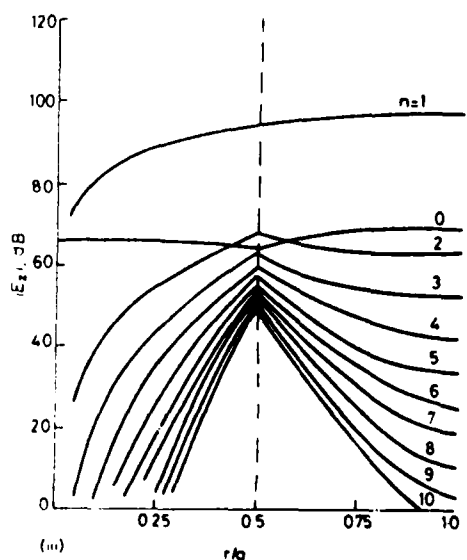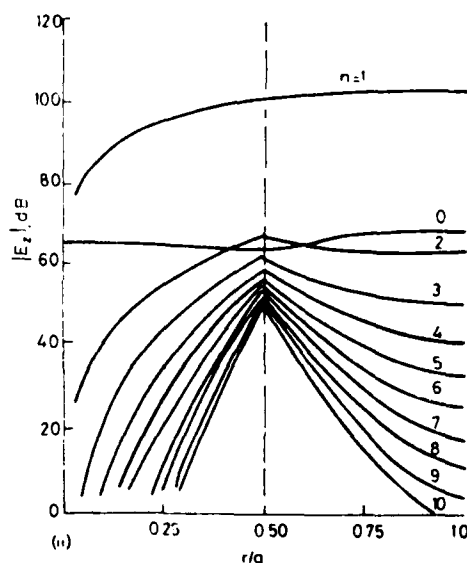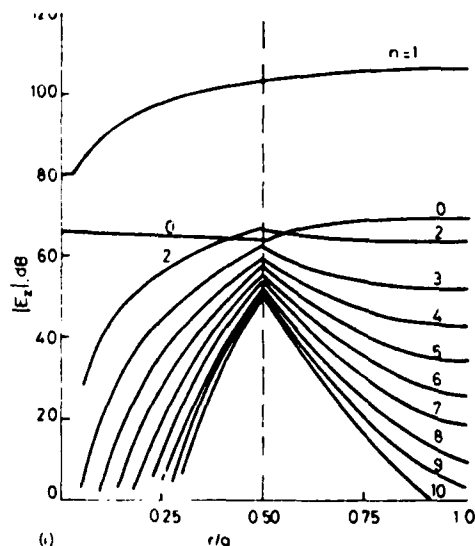
Fig. 2

Strength of electric fields of first 11 modes excited inside antenna

$a = 1.88$ cm, $b = 0.94$ cm, $d = 0.16$ cm, $\epsilon_1 = 2.47\epsilon_0$
(i) $f = 2.833$ GHz
(ii) $f = 2.805$ GHz
(iii) $f = 2.750$ GHz

where W_e and W_m are time-average stored electric and magnetic energies,

$$V = \int_0^d E_z \, dz$$

and $P_T = P_{rad} + P_D + P_L$, with P_D and P_L being the power lost in dielectric substrate, and that lost as ohmic heat on the conducting plates, respectively.

Assuming that the $n = 1$ mode is dominant, the above quantities can be expressed in analytic forms:

$$V = A_1 d J_1(k_1 b)$$

$$P_{rad} = \tfrac{1}{2} \pi a d |B_1 J_1(k_1 a) + C_1 Y_1(k_1 a)|^2 g_{a1}$$

$$P_L = 2\omega W_m d_s / d$$

$$P_D = 2\omega \tan \delta \, W_e$$

$$W_e = \frac{\pi \epsilon_1 d}{8 k_1^2} \{ |A_1|^2 [x^2(J_1^2 - J_0 J_2)]_0^{k_1 b}$$

$$+ |B_1|^2 [x^2(J_1^2 - J_0 J_2)]_{k_1 b}^{k_1 a}$$

$$+ |C_1|^2 [x^2(Y_1^2 - Y_0 Y_2)]_{k_1 b}^{k_1 a}$$

$$+ \tfrac{1}{2}(B_1 C_1^* + B_1^* C_1)[x^2(2J_1 Y_1 - J_0 J_2 - J_2 Y_0)]_{k_1 b}^{k_1 a} \}$$

$$W_m = \frac{\pi \epsilon_1 d}{8 k_1^2} \{ |A_1|^2 [x^2(J_0^2 + J_1^2) - 2J_1^2]_0^{k_1 b}$$

$$+ |B_1|^2 [x^2(J_0^2 + J_1^2) - 2J_1^2]_{k_1 b}^{k_1 a}$$

$$+ |C_1|^2 [x^2(Y_0^2 + Y_1^2) - 2Y_1^2]_{k_1 b}^{k_1 a}$$

$$+ \tfrac{1}{2}(B_1 C_1^* + B_1^* C_1)[x^2(J_0 Y_0 + J_1 J_1$$

$$+ J_2 Y_2) - \tfrac{1}{2} J_1 Y_1 - \tfrac{1}{2} J_1 Y_1]_{k_1 b}^{k_1 a} \}$$

where $[f]_B^A$ means $f(A) - f(B)$, $d_s = (\pi \mu \sigma f)^{-1/2}$ is the skin depth of the conducting plate at the operating frequency, σ is the conductivity of the plate, and $\tan \delta$ is the loss tangent of the dielectric substrate.

The above formulas are derived from indefinite integrals involving Bessel functions. These formulas are listed in Appendix 9.

Fig. 3 shows theoretical input impedances of circular-disc printed-circuit antennas with different driving points. Agreement with measured data[3] is seen to be good. Note that the antenna was etched on a rather thick printed-circuit board ($d/a = 0.085$). The input resistance at resonance agrees with the measured value better than the previous theory[4] does.

7 Acknowledgment

8 References

1 WATKINS, J.: 'Circular resonant structures in microstrip', Electron. Lett., 1969, 5, pp. 524–525

2 LO, Y.T., SOLOMON, D., ORE, J.R., HARRISON, D.D., and DESCHAMPS, G.A.: 'Study of microstrip antennas, microstrip phased arrays, and microstrip feed networks', RADC-TR-77-406 report, University of Illinois, Urbana, Illinois, 21st October, 1977

3 LONG, S.A., SHEN, L.C., WALTON, M.D., and ALLERDING, M.R.: 'Impedance of a circular-disc printed-circuit antenna', Electron. Lett., 1978, 14, pp. 684–686

4 LONG, S.A., SHEN, L.C., and MOREL, P.B.: 'Theory of the circular-disc printed-circuit antenna', Proc. IEE, 1978, 125, pp. 925–928

5 SHEN, L.C., LONG, S.A., ALLERDING, M.R., and WALTON, M.D.: 'Resonant frequency of a circular-disc, printed-circuit antenna', IEEE Trans., 1977, AP-25, pp. 595–596

6 COLLIN, R.E.: 'Foundations of microwave engineering' (McGraw-Hill, New York, 1966), p. 42

7 WATSON, G.N.: 'A treatise on the theory of Bessel functions' (Cambridge University Press, 1958, 2nd edn.)

8 WALTON, M.D.: 'An experimental study of the printed circuit circular disc antenna', M.S. thesis, University of Houston, Houston, Texas, 1976

9 Appendix

In deriving the formulas for W_e and W_m, the following integral formulas are used:

$$\int_x^1 [J_1(x)]^2 \, dx = \tfrac{1}{2} \{ [J_0(x)]^2 + [J_1(x)]^2 \} \tag{14}$$

$$\int x [J_1(x)]^2 \, dx = \tfrac{1}{2} \{ (x^2 + 1)[J_0(x)]^2 + (x^2 - 1)[J_1(x)]^2 \} \tag{15}$$

$$\int x [J_1(x)]^2 \, dx = \tfrac{1}{2} x^2 \{ [J_0(x)]^2 - J_0(x)J_2(x) \} \tag{16}$$
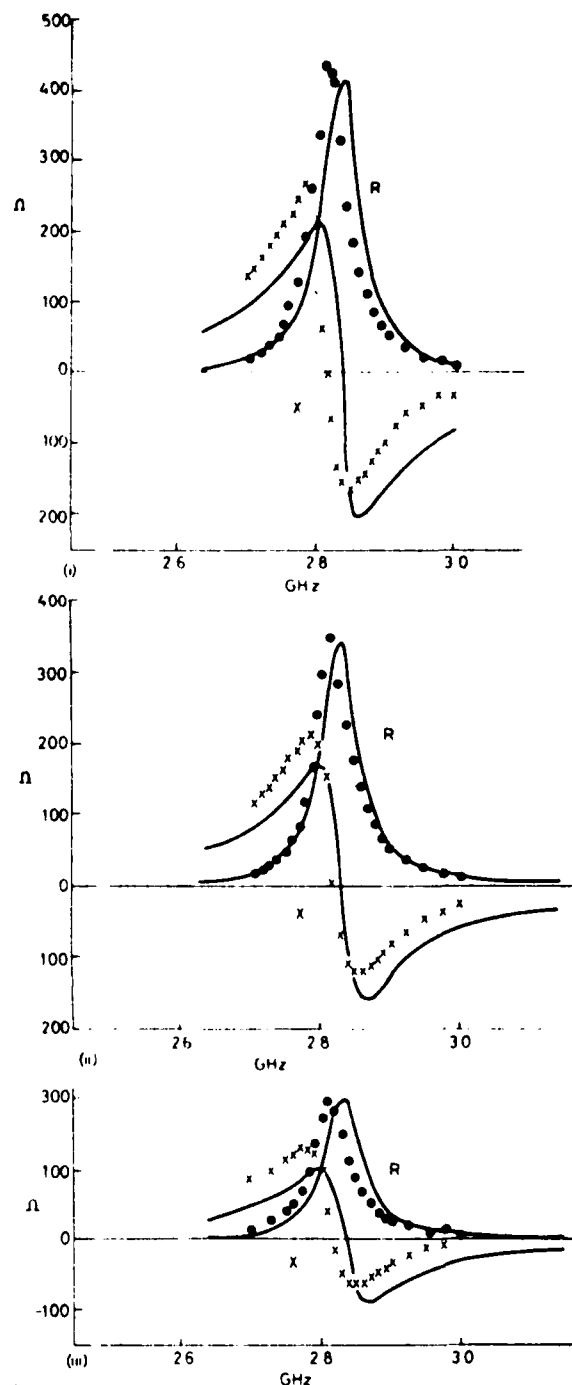
Fig. 3

Input impedances of the antenna.

$a = 1.88 \text{ cm}, d = 0.16 \text{ cm}, \epsilon_1 = 2.47\epsilon_0, \sigma = 5.8 \times 10^7 \text{ mho/m}, \tan \delta = 2 \times 10^{-3}$

(i) $b = 1.88$ cm
(ii) $b = 1.41$ cm
(iii) $b = 0.94$ cm

———— theory

xxxx ●●●● experiment

$$\int x J_1(x) Y_1(x) \, dx = \tfrac{1}{2} x^2 \{ 2J_1(x) Y_1(x) - J_0(x) Y_2(x)$$

$$- J_2(x) Y_0(x) \} \tag{17}$$

$$\int_x^1 J_1(x) Y_1(x) \, dx = \tfrac{1}{2} [J_0(x) Y_0(x) + J_1(x) Y_1(x)] \tag{18}$$

$$\int x J_1'(x) Y_1'(x) \, dx = (\tfrac{1}{2} + \tfrac{1}{2} x^2)[J_0(x) Y_0(x) + J_1(x) Y_1(x)]$$

$$+ \tfrac{1}{4} x^2 [2J_2(x) Y_2(x) - J_1(x) Y_3(x)$$

$$- J_3(x) Y_1(x)]$$

In eqns. 14–16 J may be replaced by Y. These formulas are derived or directly quoted from those in Reference 7, pp. 134–136, and from standard recurrence relations of Bessel functions.

Radiation characteristics of a circular microstrip antenna [a]

W. C. Chew and J. A. Kong

Massachusetts Institute of Technology, Department of Electrical Engineering and Computer Science, Cambridge, Massachusetts 02139

L. C. Shen

University of Houston, Department of Electrical Engineering, Houston, Texas 77004

Radiation patterns of a circular microstrip antenna have been calculated with Green's functions for a two-layer medium and compared with previous results which are valid for thin slabs and small dielectric constants. A mode expansion technique is then used to find fields and resonant frequencies. The theoretical results for the input impedances are found and are in good agreement with experimental data.

PACS numbers: 84.40.Gf

I. INTRODUCTION

A microstrip antenna consists of a metallic patch printed on top of a dielectric substrate over a highly conducting ground plane. To calculate the radiation characteristics of such a structure, we must use the field formulation for a two-layer medium, which has been a problem of historical interest.[1-5] For a circular-disk microstrip antenna, theories have been developed by using free-space Green's functions.[6] In this paper, we first calculate the radiation pattern by using the two-layer stratified medium formulation and compare with previous results[6] which are known to be valid only when the dielectric constant of the substrate is not high and when the substrate is thin as compared with the radius of the disk. We

next compute the resonant fields by using a mode expansion technique.[7,8] We show that the results obtained for the input impedances agree very well with experimental data.[9]

II. FORMULATION

Consider a microstrip antenna modelled as a current sheet placed at the interface of a dielectric slab on top of a perfectly conducting ground plane (Fig. 1). The current sheet can be represented by a current density

$$\mathbf{J}(\mathbf{r}) = \mathbf{K}(x, y)\delta(z). \tag{1}$$

The electromagnetic field components due to a point source radiating in the presence of a stratified medium have been formulated in integral forms.[5] By decomposing the current sheet into its $\hat{x}$ and $\hat{y}$ components, we can show by superposition principle that the field due to the source given by Eq. (1), with time dependence $e^{i\omega t}$ omitted, is

$$E_z = \frac{i}{8\pi\omega\epsilon} \int d^2\mathbf{r}'[\cos(\phi'+\chi)K_x + \sin(\phi'+\chi)K_y]$$
$$\times \int_{-\infty}^{\infty} dk_\rho\, k_\rho^2 (1 - R^{TM})e^{ik_z z}H_1^{(1)}(k_\rho|\boldsymbol{\rho}'-\boldsymbol{\rho}|), \tag{2}$$

$$H_z = \frac{i}{8\pi} \int d^2\mathbf{r}'[\sin(\phi'+\chi)K_x - \cos(\phi'+\chi)K_y]$$
$$\times \int_{-\infty}^{\infty} dk_\rho\, \frac{k_\rho^2}{k_z}(1 + R^{TE})e^{ik_z z}H_1^{(1)}(k_\rho|\boldsymbol{\rho}'-\boldsymbol{\rho}|), \tag{3}$$

where $k_z = (k^2 - k_\rho^2)^{1/2}$, R^{TM} and R^{TE} are, in this case, the reflection coefficients of the two-layer stratified medium and are given by (A3) and (A4), and $H_1^{(1)}(k_\rho|\boldsymbol{\rho}'-\boldsymbol{\rho}|)$ is the first-kind Hankel function of the first order. We note that the dependence of the field due to K_y is just that due to K_x rotated by 90°.

To compute the radiation pattern, we are only interested in the limit when $|\boldsymbol{\rho}-\boldsymbol{\rho}'| \to \infty$ and $z \to \infty$. In such a case, $\phi' + \chi \cong \phi$ and Eqs. (2) and (3) become

$$E_z \sim \frac{i}{8\pi\omega\epsilon} \int d^2\mathbf{r}'(\cos\phi K_x + \sin\phi K_y)$$
$$\times \int_{-\infty}^{\infty} dk_\rho\, k_\rho^2(1 - R^{TM})e^{ik_z z}H_1^{(1)}(k_\rho|\boldsymbol{\rho}'-\boldsymbol{\rho}|), \tag{4}$$

$$H_z \sim \frac{i}{8\pi} \int d^2\mathbf{r}'(\sin\phi K_x - \cos\phi K_y)$$
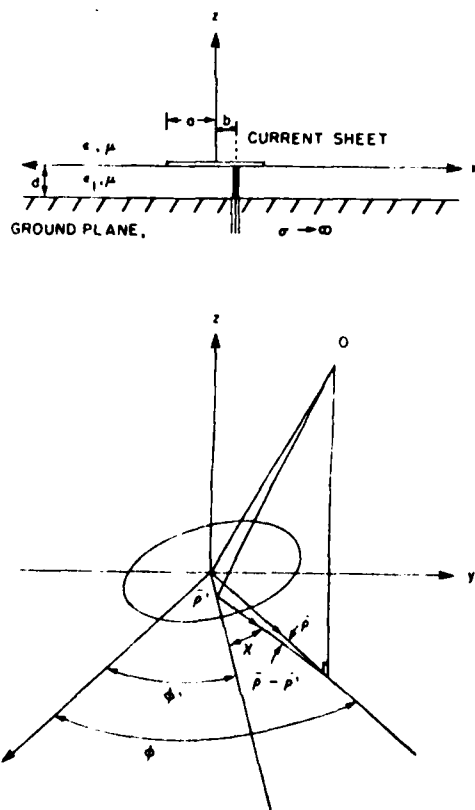
FIG. 1 Geometrical configurations of the problem.

$$\times \int_{-}^{'} dk_{\rho} \frac{k_{\rho}^{2}}{k_{z}} (1 + R^{''}) e^{ik_{z}'} H_{1}^{(1)}(k_{\rho}|\boldsymbol{\rho}' - \boldsymbol{\rho}|).$$

(5)

The other components of E and H fields can be derived from Eqs. (2) and (3). By using the steepest descent method, it can be shown that the electric field components in the far field are given by

$$E_{z} = -\frac{i}{4\pi\omega\epsilon} k^{2} \sin\theta \cos\theta \left[1 - R^{1M}(\theta)\right] \frac{e^{ikr}}{r}$$
$$\times \int d^{2}\mathbf{r}'(\cos\phi K_{x} + \sin\phi K_{y}) e^{-ik\cdot\boldsymbol{\rho}},$$

(6)

$$E_{\rho} = \frac{i}{4\pi\omega\epsilon} k^{2} \cos^{2}\theta \left[1 - R^{1M}(\theta)\right] \frac{e^{ikr}}{r}$$
$$\times \int d^{2}\mathbf{r}'[\cos\phi K_{x} + \sin\phi K_{y}] e^{-ik\cdot\boldsymbol{\rho}},$$

(7)

$$E_{\phi} = \frac{\omega\mu}{4\pi i} \left[1 + R^{''}(\theta)\right] \frac{e^{ikr}}{r}$$
$$\times \int d^{2}\mathbf{r}'(\sin\phi K_{x} - \cos\phi K_{y}) e^{-ik\cdot\boldsymbol{\rho}}.$$

(8)

In the above, we have omitted the singularity contributions in the steepest descent approach, which can be shown to be negligible (see Appendix A). We also notice that the far field approximation of the field is similar to that due to a current sheet in free space except now that the TM waves are scaled by a factor $[1 - R^{1M}(\theta)]$ and the TE waves by a factor $[1 + R^{''}(\theta)]$.

III. RADIATION PATTERNS DUE TO A CIRCULAR DISK ANTENNA

To find the radiation pattern due to modes excited on a circular disk antenna printed on a microstrip board, we need to know the current distribution on the disk for various modes. The approximation to the current distribution can be obtained by studying the modes of a circular cavity surrounded by a cylindrical magnetic wall. For such a cavity, the field inside is given by[10]

$$E_{z} = E_{0} J_{n} \left[(\beta_{nm}/a)\rho\right] \cos n\phi,$$

(9a)

$$H_{\rho} = \frac{i\omega_{nm}\epsilon_{1}n}{(\beta_{nm}/a)^{2}\rho} E_{0} J_{n}\left(\frac{\beta_{nm}}{a}\rho\right) \sin n\phi,$$

(9b)

$$H_{\phi} = \frac{i\omega_{nm}\epsilon_{1}}{(\beta_{nm}/a)} E_{0} J_{n}'\left(\frac{\beta_{nm}}{a}\rho\right) \cos n\phi,$$

(9c)

where

$$\omega_{nm} = \beta_{nm}/[a(\mu_{1}\epsilon_{1})^{1/2}].$$

Since the tangential H field has to vanish on the magnetic wall, $H_{\phi}(r = 0) = 0$ or $J_{n}'(\beta_{nm}) = 0$, where a is a radius of the cavity. The current distribution on the cavity wall is given by

$$\mathbf{K} = \hat{n} \times \mathbf{H} = -H_{\rho}\hat{\phi} + H_{\phi}\hat{\rho}.$$

(10)

Therefore the current distribution for various modes is given by

$$K_{\phi} = -\frac{i\omega_{nm}\epsilon_{1}n}{(\beta_{nm}/a)^{2}\rho} E_{0} J_{n}\left(\frac{\beta_{nm}}{a}\rho\right) \sin n\phi,$$

(11a)

$$K_{\rho} = \frac{i\omega_{nm}\epsilon_{1}}{(\beta_{nm}/a)} E_{0} J_{n}'\left(\frac{\beta_{nm}}{a}\rho\right) \cos n\phi.$$

(11b)

We can assume Eq. (11) to be the zeroth order approximation to the current distribution of a circular microstrip antenna and use it to calculate the radiation pattern.

Substituting Eq. (11) into Eqs. (7) and (8) (see Appendix B), we obtain

$$E_{\theta} = \omega\mu(\epsilon_{1}/\mu_{1})^{1/2} \frac{e^{ikr}}{2r} (-i)^{n+1}$$
$$\times E_{0} \cos\theta \cos n\phi \frac{(\beta_{nm}/a)}{(\beta_{nm}/a)^{2} - k^{2}\sin^{2}\theta}$$
$$\times [aJ_{n}(\beta_{nm})J_{n}'(ka\sin\theta)][1 - R^{1M}(\theta)],$$

(12)

$$E_{\phi} = \omega\mu(\epsilon_{1}/\mu_{1})^{1/2} \frac{e^{ikr}}{2r} n(-i)^{n+1} \frac{E_{0} \sin n\phi}{(\beta_{nm}/a)k\sin\theta}$$
$$\times J_{n}(\beta_{nm})J_{n}(ka\sin\theta)[1 + R^{''}(\theta)].$$

(13)

When $n = 1$, the mode has the lowest resonant frequency and has been extensively studied. In Figs. 2 and 3, we plot the radiation field when $\omega = \omega_{nm}$ for different $\epsilon_{r} = (\epsilon_{1}/\epsilon)$ and d/a ratios. The electric fields are normalized with respect to $rE_{0}aJ_{n}(\beta_{nm})$. Long et al.[6] calculated the radiation field by assuming magnetic current sheet on the side wall of the cavity and using free-space Green's function. Their results are plotted in dotted curves for comparison. We note that when d/a is small, both result agree very well except for $\theta \sim 90°$. Since their formula does not account for the dielectric effect of the substrate, we conclude that the dielectric effect on the
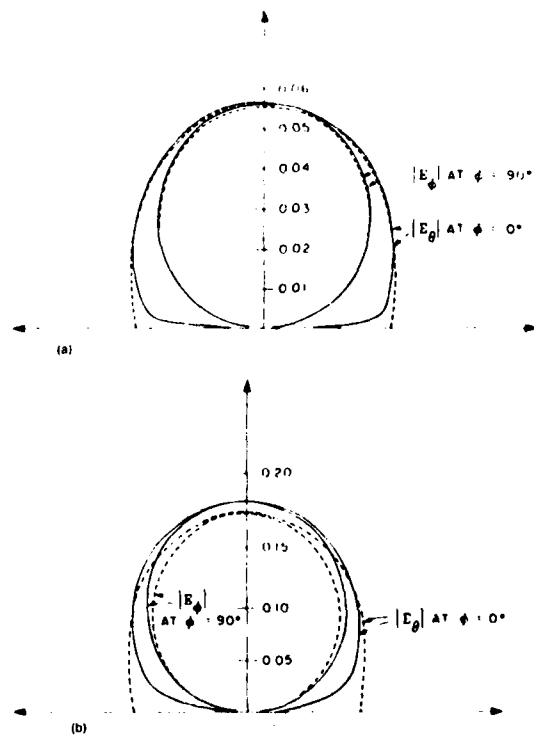

FIG. 2. Radiation patterns due to $n = 1$ mode for $\epsilon_{r} = 2.65$ and $k_{1}a = 1.841\,18$. The dotted curves are from Long et al. for comparison. (a) $d/a = 0.1$, (b) $d/a = 0.3$.

FIG. 3. Radiation patterns due to $n = 1$ mode for $\epsilon_r = 9.6$ and $k_0 a = 1.84118$. The dotted curves are from Long et al. for comparison. (a) $d/a = 0.1$, (b) $d/a = 0.3$
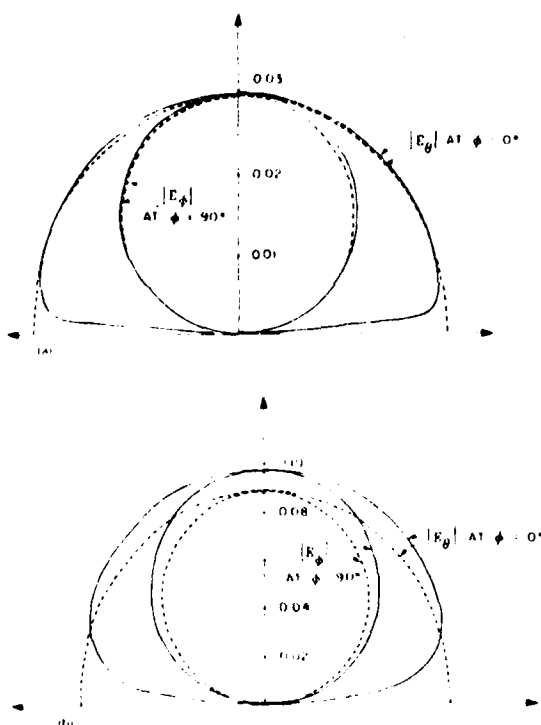
radiation field is small when d/a is small. However, when d/a is large, noted discrepancies are observed. These discrepancies are larger when ϵ_r is increased. We find that the radiation field increases in intensity when d/a increases. Also the directivity in the normal direction improves when d/a increases and ϵ_r decreases. When ϵ_r is large or d/a small, more power is directed near the horizontal direction.

An additional effect of the dielectric is the presence of a guided surface wave that carries power only in the horizontal direction at $\theta = 90°$. However, when the microstrip disk is mounted on a finite-size ground plane, this guided wave can be diffracted into other angles and gives rise to radiated power. When the dielectric layer or the ground plane is lossly, the guided wave has a complex wave number [see Eq. (A6)]. In such cases, the guided wave decays exponentially away from the source as its power is dissipated in the dielectric layer or ground plane.

IV. MODE EXCITATION OF A MICROSTRIP DISK BY A PROBE

In the limit of small d, the microstrip disk acts like a high Q resonator and the field inside the disk resonator resembles that of a closed resonator with a magnetic wall on the side.[10] The modes of the resonator cavity can be divided into the natural modes and the unnatural modes,[7,8] in terms of which arbitrary E and H field can be expanded. We write

$$\mathbf{E} = \sum_{n,m,p} e_{nmp}\mathbf{E}_{nmp} + \sum_{n,m,p} f_{nmp}\mathbf{F}_{nmp}, \tag{14a}$$

$$\mathbf{H} = \sum_{n,m,p} h_{nmp}\mathbf{H}_{nmp} + \sum_{n,m,p} g_{nmp}\mathbf{G}_{nmp}, \tag{14b}$$

where n denotes the ϕ variation m the ρ variation, and p the z variation of the field. In the above, $\{\mathbf{E}_{nmp},\mathbf{H}_{nmp}\}$ forms the natural mode and $\mathbf{F}_{nmp}$ is the unnatural mode for the electric field, and $\mathbf{G}_{nmp}$ is the unnatural mode for, the magnetic field. The natural mode fields satisfy the following equations:

$$\nabla \times \mathbf{E}_{nmp} = k_{nmp}\mathbf{H}_{nmp}, \quad \nabla \times \mathbf{H}_{nmp} = k_{nmp}\mathbf{E}_{nmp} \tag{15a}$$

$$(\nabla^2 + k_{nmp}^2)\binom{\mathbf{E}_{nmp}}{\mathbf{H}_{nmp}} = 0 \tag{15b}$$

and the boundary conditions

$$\hat{n} \times \mathbf{E}_{nmp} = 0, \quad \text{on } S_e, \quad \hat{n}\cdot\mathbf{E}_{nmp} = 0, \quad \text{on } S_m$$
$$\hat{n}\cdot\mathbf{H}_{nmp} = 0, \quad \text{on } S_e, \quad \hat{n}\times\mathbf{H}_{nmp} = 0, \quad \text{on } S_m, \tag{15c}$$

where S_e indicates the electric conductor surface and S_m the side magnetic wall. The unnatural mode for the electric field satisfies

$$k_{nmp}\mathbf{F}_{nmp} = \nabla\psi_{nmp}, \tag{16a}$$

where

$$(\nabla^2 + k_{nmp}^2)\psi_{nmp} = 0 \tag{16b}$$

and the boundary conditions

$$\psi_{nmp} = \text{const } 1, \quad \text{on } S_u$$
$$= \text{const } 2, \quad \text{on } S_l$$

and

$$\frac{\partial\psi_{nmp}}{\partial\rho} = 0 \quad \text{on } S_m, \tag{16c}$$

where S_u is the top conducting disk of the cavity and S_l the bottom conducting disk. Since $\nabla\cdot\mathbf{F}_{nmp} = (1/k_{nmp})\nabla^2\psi_{nmp} = -k_{nmp}\psi_{nmp}$, we see that if $k_{nmp} \neq 0$, the electric field $\mathbf{F}_{nmp}$ corresponds to the field due to static electric charge distribution $\rho_l = -\epsilon_l k_{nmp}\psi_{nmp}$ permeating the cavity.

The unnatural mode for the magnetic field satisfies

$$k_{nmp}\mathbf{G}_{nmp} = \nabla\phi_{nmp}, \tag{17a}$$

where

$$(\nabla^2 + k_{nmp}^2)\phi_{nmp} = 0 \tag{17b}$$

and the boundary conditions

$$\phi_{nmp} = 0, \quad \text{on } S_m$$

and

$$\frac{\partial\phi_{nmp}}{\partial z} = 0, \quad \text{on } S_e. \tag{17c}$$

We find that $\nabla\cdot\mathbf{G}_{nmp} = -k_{nmp}\phi_{nmp}$, which implies that the magnetic field $\mathbf{G}_{nmp}$ corresponds to field due to static magnetic charge distribution $\rho_m = -\mu_l k_{nmp}\phi_{nmp}$. Since

$$\nabla \times \binom{\mathbf{F}_{nmp}}{\mathbf{G}_{nmp}} = 0,$$

the unnatural modes are also termed the irrotational modes.

To solve for e_{nmp}, h_{nmp}, we make use of the identity[7]

$$\int_V \nabla\cdot(\mathbf{E}\times\mathbf{H}_{nmp})\,dV$$
$$= \int_V (\nabla\times\mathbf{E})\cdot\mathbf{H}_{nmp}\,dV - \int_V (\nabla\times\mathbf{H}_{nmp})\cdot\mathbf{E}\,dV$$

$$\int_{S} \hat{n} \times \mathbf{E} \cdot \mathbf{H}_{nmp}\, dS, \tag{18a}$$

the relations $\nabla \times \mathbf{H}_{nmp} = k_{nmp}\mathbf{E}_{nmp}$ and $\nabla \times \mathbf{E} = i\omega\mu_1\mathbf{H}$, and the mode orthogonality properties to obtain

$$i\omega\mu_1 h_{nmp} - k_{nmp}e_{nmp} = \int_{S} \hat{n} \times \mathbf{E} \cdot \mathbf{H}_{nmp}\, dS. \tag{18b}$$

Similarly, using

$$\int_{V} \nabla \cdot (\mathbf{E}_{nmp} \times \mathbf{H})\, dV$$

$$= \int_{V} (\nabla \times \mathbf{E}_{nmp} \cdot \mathbf{H} - \nabla \times \mathbf{H} \cdot \mathbf{E}_{nmp})\, dV$$

$$= \int_{S} \hat{n} \times \mathbf{H} \cdot \mathbf{E}_{nmp}\, dS \tag{19a}$$

and the Maxwell equations $\nabla \times \mathbf{H} = -i\omega\epsilon_1\mathbf{E} + \mathbf{J}$, $\nabla \times \mathbf{E}_{nmp} = k_{nmp}\mathbf{H}_{nmp}$, we arrive at

$$k_{nmp}h_{nmp} + i\omega\epsilon_1 e_{nmp} - \int_{V} \mathbf{J} \cdot \mathbf{E}_{nmp}\, dV$$

$$= -\int_{S} \hat{n} \times \mathbf{H} \cdot \mathbf{E}_{nmp}\, dS. \tag{19b}$$

To solve for f_{nmp}, we make use of

$$\int_{V} (\mathbf{H} \cdot \nabla \times \mathbf{F}_{nmp} - \mathbf{F}_{nmp} \cdot \nabla \times \mathbf{H})\, dV$$

$$= \int_{S} \hat{n} \times \mathbf{H} \cdot \mathbf{F}_{nmp}\, dS \tag{20a}$$

to obtain

$$i\omega\epsilon_1 f_{nmp} = \int_{V} \mathbf{J} \cdot \mathbf{F}_{nmp}\, dV - \int_{S} \hat{n} \times \mathbf{H} \cdot \mathbf{F}_{nmp}\, dS. \tag{20b}$$

For g_{nmp}, we make use of

$$\int_{V} (\mathbf{G}_{nmp} \cdot \nabla \times \mathbf{E} - \mathbf{E} \cdot \nabla \times \mathbf{G}_{nmp})\, dV = \int_{S} \hat{n} \times \mathbf{E} \cdot \mathbf{G}_{nmp}\, dS \tag{21a}$$

to get

$$i\omega\mu g_{nmp} = \int_{S} \hat{n} \times \mathbf{E} \cdot \mathbf{G}_{nmp}\, dS. \tag{21b}$$

Equations (18b), (19b), (20b), and (21b) can be solved approximately, if ω is such that $\omega^2\mu_1\epsilon_1 \simeq k_{nmp}^2$. In such a case, we get $\mathbf{E} \sim e_{nmp}\mathbf{E}_{nmp}$, $\mathbf{H} \sim h_{nmp}\mathbf{H}_{nmp}$. Hence the left-hand side of (18b)–(21b) can be approximated. We have from (18b) that

$$\int_{S} \hat{n} \times \mathbf{E} \cdot \mathbf{H}_{nmp}\, dS \approx Z_s h_{nmp} \int_{S} |\mathbf{H}_{nmp}|^2\, dS, \tag{22a}$$

where Z_s is the surface impedance of the metallic surface given by $Z_s = (1 - i)/\sigma\delta_s$. Since the real power dissipated on the metallic surface is given by

$$P_{d_{nmp}} = \frac{1}{2\sigma\delta_s} \int_{S} |\mathbf{H}_{nmp}|^2\, dS,$$

and the Q due to this loss is

$$Q_{d_{nmp}} = \frac{\omega\mu_1 \int_{V} |\mathbf{H}_{nmp}|^2\, dV}{2P_{d_{nmp}}} = \frac{\omega\mu_1}{2P_{d_{nmp}}},$$

we have

$$\int_{S} \hat{n} \times \mathbf{E} \cdot \mathbf{H}_{nmp}\, dS \cong \frac{\omega\mu_1}{Q_{d_{nmp}}} h_{nmp}(1 - i). \tag{22b}$$

From (19b), we can simplify the right-hand side as

$$\int_{S} \hat{n} \times \mathbf{H} \cdot \mathbf{E}_{nmp}\, dS \cong Y_m e_{nmp} \int_{S_m} |\mathbf{E}_{nmp}|^2\, dS, \tag{23a}$$

where Y_m is the surface admittance of the surface S_m. In essence, we have replaced the surface S_m with a lossy magnetic wall. In general, $Y_m = G_m(1 - i\alpha)$, where α is nonunity. Similarly, we can relate (23a) to the Q due to the magnetic wall loss and have

$$-\int_{S} \hat{n} \times \mathbf{H} \cdot \mathbf{E}_{nmp}\, dS \sim \frac{\omega\epsilon_1}{Q_{r_{nmp}}} e_{nmp}(1 - i\alpha), \tag{23b}$$

where

$$Q_{r_{nmp}} = \frac{\omega\epsilon_1 \int_{V} |\mathbf{E}_{nmp}|^2\, dV}{2P_{r_{nmp}}} = \frac{\omega\epsilon_1}{2P_{r_{nmp}}} \tag{23c}$$

is the Q associated with the radiated power loss $P_{r_{nmp}}$ of the nmp mode.

Therefore (18b) and (19b) can be solved for e_{nmp} and h_{nmp} giving

$$e_{nmp} \approx \frac{i\omega\mu_1[1 + (1 + i)/Q_{d_{nmp}}]\int_{V} \mathbf{J} \cdot \mathbf{E}_{nmp}\, dV}{k_{nmp}^2 - \omega^2\mu_1\epsilon_1[1 + (1 + i)/Q_{d_{nmp}}][1 + (\alpha + i)/Q_{r_{nmp}}]}, \tag{24}$$

$$h_{nmp} \approx \frac{k_{nmp}\int_{V} \mathbf{J} \cdot \mathbf{E}_{nmp}\, dV}{k_{nmp}^2 - \omega^2\mu_1\epsilon_1[1 + (1 + i)/Q_{d_{nmp}}][1 + (\alpha + i)/Q_{r_{nmp}}]}. \tag{25}$$

Noting that the second term on the right-hand side of (20b) is small, we have

$$f_{nmp} \approx \frac{1}{i\omega\epsilon_1} \int_{V} \mathbf{J} \cdot \mathbf{F}_{nmp}\, dV \tag{26}$$

and also that

$$g_{nmp} \approx 0. \tag{27}$$

We shall assume that the current source due to the probe, when $d \ll \lambda$, is given by

$$\mathbf{J} = \hat{z}I\delta(x - b)\delta(y), \quad 0 < z < d. \tag{28}$$

We see that due to the uniformity of the current on the probe along z, only the $\mathbf{E}_{nm0}$, $\mathbf{H}_{nm0}$, and $\mathbf{F}_{nm0}$ modes will be excited, that

$$\mathbf{J} = \hat{z} Id\delta(x - b)\delta(y), \quad 0 < z < d. \tag{28}$$

We see that due to the uniformity of the current on the probe along z, only the $\mathbf{E}_{nmo}$, $\mathbf{H}_{nmo}$, and $\mathbf{F}_{nmo}$ modes will be excited, that is, only modal fields with no z variation are excited. Since the current probe has uniform current distribution, there is no charge accumulation in the cavity. Thus

if can be shown that no $\mathbf{F}_{nmo}$ modes are excited. Similarly, since all the TE modes of the cavity have z variation, none of them are excited. As such, the natural mode of the magnetic wall cavity which is of interest is the TM mode, whose field is given by

$$\mathbf{E}_{nmo} = \hat{z} E_{nmo} J_n [(\beta_{nm}/a)\rho] \cos n\phi, \tag{29a}$$

where $J_n'(\beta_{nm}) = 0$. We have assumed that the probe is placed at $\phi = 0$ so that E_{nmo} is an even function of ϕ. The magnetic field of the natural mode can be derived using (15a) giving

$$\mathbf{H}_{nmo} = -E_{nmo}\left[\hat{\rho} - \frac{n}{(\beta_{nm}/a)\rho} J_n\left(\frac{\beta_{nm}}{a}\rho\right)\sin n\phi + \hat{\phi} J_n'\left(\frac{\beta_{nm}}{a}\rho\right)\cos n\phi\right]. \tag{29b}$$

In the above, E_{nmo} is a normalizing constant such that

$$\int_v |\mathbf{E}_{nmo}|^2 \, dV = \int_v |\mathbf{H}_{nmo}|^2 \, dV = 1. \tag{30}$$

Thus E_{nmo} can be derived easily.

$$E_{nmo} = (2/\pi d)^{1/2} \frac{\beta_{nm}}{a J_n(\beta_{nm})} \frac{(1 - \tfrac{1}{2}\delta_{0n})^{1/2}}{(\beta_{nm}^2 - n^2)^{1/2}}. \tag{31}$$

Also k_{nmo} in Eq. (15) is given by (β_{nm}/a) in this case. Using the above, we find that

$$\int_v \mathbf{J} \cdot \mathbf{E}_{nmo} \, dV = E_{nmo} J_n\left(\frac{\beta_{nm}}{a} b\right) Id. \tag{32}$$

Thus we conclude that

$$\mathbf{E} \simeq \hat{z} \frac{i\omega\mu_1 Id\left[1 + (1 + i)/Q_{d_{nmo}}\right] E_{nmo}^2 J_n[(\beta_{nm}/a)b]}{(\beta_{nm}/a)^2 - \omega^2\mu_1\epsilon_1[1 + (1 + i)/Q_{d_{nmo}}][1 + (\alpha + i)/Q_{r_{nmo}}]} J_n\left(\frac{\beta_{nm}}{a}\rho\right)\cos n\phi \tag{33}$$

and

$$\mathbf{H} \simeq \frac{Idk_{nmo} E_{nmo}^2 J_n[(\beta_{nm}/a)b]}{(\beta_{nm}/a)^2 - \omega^2\mu_1\epsilon_1[1 + (1 + i)/Q_{d_{nmo}}][1 + (\alpha + i)/Q_{r_{nmo}}]}$$
$$\times \left[\hat{\rho}\frac{n}{(\beta_{nm}/a)\rho} J_n\left(\frac{\beta_{nm}}{a}\rho\right)\sin n\phi + \hat{\phi} J_n'\left(\frac{\beta_{nm}}{a}\rho\right)\cos n\phi\right], \tag{34}$$

when $k_{nmo}^2 \sim \omega^2\mu_1\epsilon_1$. This is true when $Q_{d_{nmo}} \gg 1$ and $Q_{r_{nmo}} \gg 1$. The resonant frequency of the disk is given when the denominators of (33) and (34) vanish. Thus the resonant frequency for the nmo mode is given by

$$\omega_{nmo} = \frac{\beta_{nm}}{(\mu_1\epsilon_1)^{1/2}a}\left[\left(1 + \frac{1 + i}{Q_{d_{nmo}}}\right)\left(1 + \frac{\alpha + i}{Q_{r_{nmo}}}\right)\right]^{-1/2}$$
$$\simeq \frac{\beta_{nm}}{(\mu_1\epsilon_1)^{1/2}a}\left(1 - \frac{1 + i}{2Q_{d_{nmo}}} - \frac{\alpha + i}{2Q_{r_{nmo}}}\right). \tag{35}$$

The frequency shift from the magnetic wall model is due to real and reactive power absorbed by the metallic wall and real and reactive power leaking out of the disk resonator. $Q_{d_{nmo}}$ can be computed since we can compute $P_{d_{nmo}}$, the power dissipated on the metallic surface due to the mno mode.

We can also compute $Q_{r_{nmo}}$ through $P_{r_{nmo}}$, the real power radiated by the disk. We note that $(1 - i\alpha)P_{r_{nmo}}$ is the complex power leaking out of the disk resonator through the side aperture. This power includes the power in the guided surface wave and spherical wave radiating into infinity. Thus this power is also dissipated in the dielectric loss and copper loss outside the cavity. The reason there is complex power leaving the cavity is because of the actual nonvanishing tangential H field at the aperture of the cavity. To find a first-order approximation to this nonvanishing tangential H field, we assume a current distribution on the disk due to a natural mode given by

$$K_\phi = \frac{E_{nmo}}{i\omega\mu_1}\frac{n}{\rho} J_n\left(\frac{\beta_{nm}}{a}\rho\right)\sin n\phi, \tag{36a}$$

$$K_\rho = \frac{E_{nmo}}{i\omega\mu_1}\frac{\beta_{nm}}{a} J_n'\left(\frac{\beta_{nm}}{a}\rho\right)\cos n\phi. \tag{36b}$$

Using the stratified medium formalism, it can be shown that this current source gives rise to nonvanishing tangential H field at the aperture given by

$$H_\phi^{(1)} = \cos n\phi \left(\frac{\mu n}{\mu_1 \rho} \int_0^\infty \frac{h_n(k_\rho) k_{1z} \cos k_{1z}(z+d)}{k_\rho \sin k_{1z} d} (1 + R^{\mathrm{TE}}) J_n(k_\rho, \rho) \, dk_\rho \right.$$
$$\left. - i\omega\epsilon \int_0^\infty e_n(k_\rho) \frac{\cos k_{1z}(z+d)}{\cos k_{1z} d} (1 + R^{\mathrm{TM}}) J_n'(k_\rho, \rho) \, dk_\rho \right), \tag{37}$$

where

$$h_n(k_\rho) = -\frac{nE_{nm\sigma}}{2k_z \omega \mu_1} J_n(\beta_{nm}) J_n(k_\rho a), \tag{37a}$$

$$e_n(k_\rho) = -\frac{E_{nm\sigma} k_\rho \beta_{nm}^2}{\omega^2 \mu_1 \epsilon a [(\beta_{nm}/a)^2 - k_\rho^2]} J_n(\beta_{nm}) J_n'(k_\rho a). \tag{37b}$$

Thus an approximation to $P_{r_{-}}(1 - i\alpha)$ is, from (23b) and (23c), given by

$$P_{r_{-}}(1 - i\alpha) = -\frac{1}{2} \int_{S_-} \hat{n} \times \mathbf{H} \cdot \mathbf{E}_{nmp} \, dS$$
$$\simeq -\frac{1}{2} \int_d^0 \int_0^{2\pi} E_{nm\sigma z} H_\phi^{(1)} \Big|_{\rho = a} \, a d\phi \, dz = \frac{\pi E_{nm\sigma}^2 \beta_{nm}^2}{4i\omega\mu_1} J_n^2(\beta_{nm}) F(\omega)(1 + \delta_{0n}), \tag{38}$$

where $F(\omega)$ is given by

$$F(\omega) = \frac{i\mu n^2}{\mu_1 \beta_{nm}^2} \int_0^\infty \frac{J_n^2(k_\rho a)}{k_\rho k_z} (1 + R^{\mathrm{TE}}) \, dk_\rho + \int_0^\infty k_\rho \frac{[J_n'(k_\rho a)]^2}{[(\beta_{nm}/a)^2 - k_\rho^2]} \frac{\tan k_{1z} d}{k_{1z}} (1 + R^{\mathrm{TM}}) \, dk_\rho. \tag{38a}$$

Consequently, we find, with the use of Eq. (31), that

$$\frac{\alpha + i}{Q_{r_{-}}} \simeq \left(\frac{\beta_{nm}^2}{ak_1} \right)^2 \frac{\beta_{nm}^2}{d[\beta_{nm}^2 - n^2]} F(\omega), \tag{38b}$$

which can be used in Eqs. (33) and (34) to find **E** and **H**. The integral in (38a) can be integrated along the Sommerfeld integration path numerically. The above approach is similar to the perturbation approach used in finding the resonant frequency shift of a microstrip disk resonator.[11,12]

V. INPUT IMPEDANCE

After having studied the modal excitation of the microstrip cavity, we can compute the input impedance of the antenna quite easily. First we find the complex power P delivered to the microstrip cavity which is given by

$$P = -\int_V \mathbf{E} \cdot \mathbf{J}^* \, dV. \tag{39}$$

Since P is also given by

$$P = Z_{in} |I|^2, \tag{40}$$

making use of Eqs. (28) and (33), we find that

$$Z_{in} = -\frac{i\omega\mu d^2 [1 + (1 + i)/Q_{d_{nm}}] E_{nm\sigma}^2 J_n^2 [(\beta_{nm}/a)b]}{(\beta_{nm}/a)^2 - \omega^2\mu_1\epsilon_1 [1 + (1 + i)/Q_{d_{nm}}][1 + (\alpha + i)/Q_{r_{nm}}]}. \tag{41a}$$

The above can be simplified to

$$Z_{in} = -\frac{i\omega\mu d J_n^2 [(\beta_{nm}/a)b](\beta_{nm}/a)^2 [1 + (1 + i)/Q_{d_{nm}}](2 - \delta_{0n})}{\pi\{(\beta_{nm}/a)^2 - \omega^2\mu_1\epsilon_1 [1 + (1 + i)/Q_{d_{nm}}][1 + (\alpha + i)/Q_{r_{nm}}]\}(\beta_{nm}^2 - n^2) J_n^2(\beta_{nm})}. \tag{41b}$$

In Figs. 4(a), 4(b), and 4(c), we plot the conjugate of the input impedance using Eqs. (41) and compare the results with experimental data.[9] (The conjugate of impedance was plotted because we have used $e^{-i\omega t}$ in our analysis.) We find that we can match the input resistance very well. Also, we have slightly altered ϵ_r from the manufacturer's specifications. This is done in order to line up the resonant frequency with that found by experiment. Since ϵ_r was specified to be 2.47 + 0.04 in the range of 8–12.5 GHz, it was uncertain that ϵ_r remained within the range at 3 GHz. Also we find that our approximation to the reactance is not as good as predicted by experiment. This is because X arises out of the energy stored

in the near field of the driving source. Since we have used a single-mode approximation, this near field, which is singular, is crudely approximated.

From Eq. (41) we notice that when the Q of the resonator is low, the bandwidth of the microstrip antenna is larger. It thus seems that a way to increase the bandwidth of the antenna is to increase the radiation loss by increasing d/a ratio.
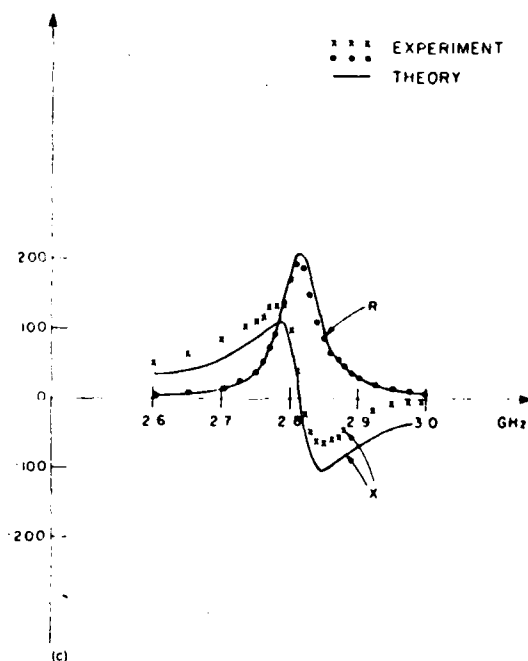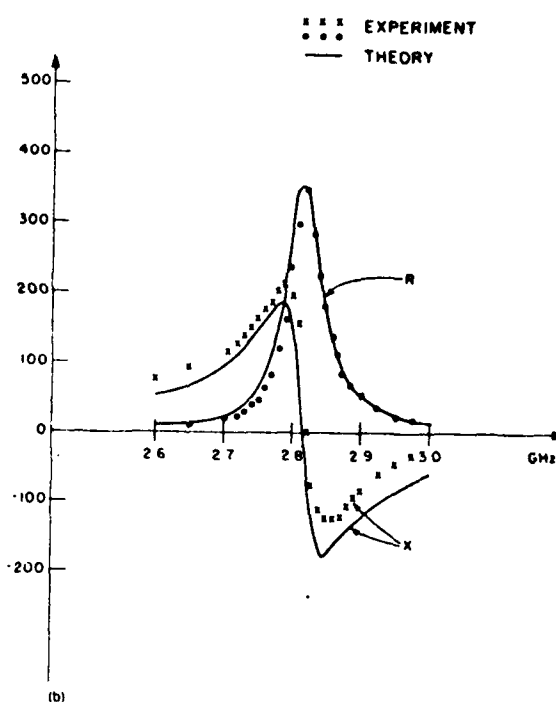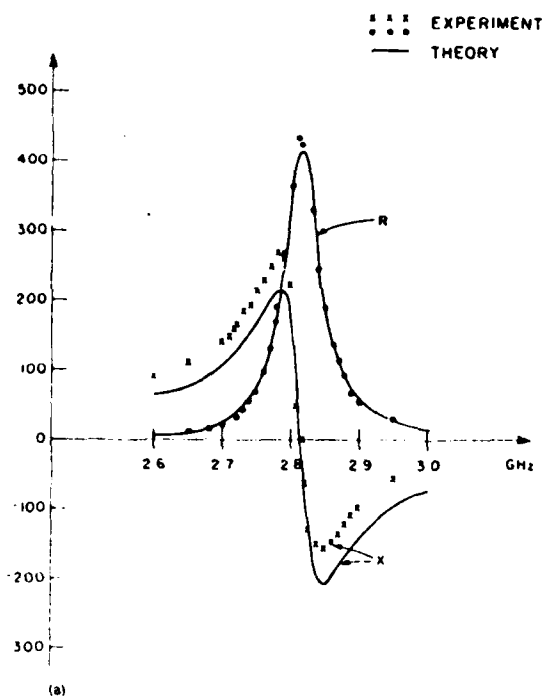
FIG. 4. Input impedance compared with experimental data. Theoretical curves are plotted for $d = 0.16$ cm, $a = 1.88$ cm, $\epsilon_r = 2.60$, $n = 1$, $\sigma = 5.8 \times 10^7$ mho/m, and loss tangent $= 1.8 \times 10^{-3}$. (a) $b = 1.88$ cm, (b) $b = 1.41$ cm, (c) $b = 0.94$ cm.

APPENDIX A: INTEGRAL APPROXIMATION BY THE STEEPEST DESCENT METHOD

In the text of this paper, we can simplify integrals (4) and (5) provided that we can simplify the following integrals:

$$I_1 = \int_{-\infty}^{\infty} dk_\rho \, \frac{k_\rho}{k_z} (1 - R^{1M}) e^{ik_z z} H_0^{(1)}(k_\rho |\boldsymbol{\rho}' - \boldsymbol{\rho}|) \tag{A1}$$

$$I_2 = \int_{-\infty}^{\infty} dk_\rho \, \frac{k_\rho}{k_z} (1 + R^{1E}) e^{ik_z z} H_0^{(1)}(k_\rho |\boldsymbol{\rho}' - \boldsymbol{\rho}|). \tag{A2}$$

The inner integrals in (4) and (5) are just derivatives of I_1 or I_2. For a stratified medium shown in Fig. 1,

$$1 - R^{1M} = \frac{1 - e^{i2k_{1z} d}}{1 + R_{01}^{1M} e^{i2k_{1z} d}} (-R_{01}^{1M})$$

$$\frac{2 \sin k_{1z} d}{\sin k_{1z} d + i(\epsilon_1/\epsilon)(k_z/k_{1z}) \cos k_{1z} d}, \tag{A3}$$
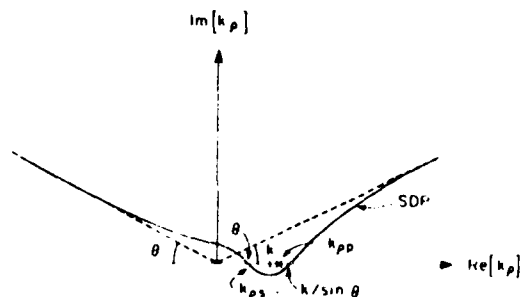
FIG. A1 The steepest descent path (SDP), the stationary point (k_{ps}), the branch point (k), and the pole (k_{pp}) on the complex k_p plane.

$$1 + R^{11} = \frac{1 - e^{i2k_{1z}d}}{1 - R_{01}^{11}e^{i2k_{1z}d}}(1 + R_{01}^{11})$$

$$= \frac{2 \sin k_{1z}d}{\sin k_{1z}d + i(\mu/\mu_1)(k_{1z}/k_z)\cos k_{1z}d}, \quad (A4)$$

where $k_{1z} = (k_1^2 - k_p^2)^{1/2}$. The locations of the poles are given by the transcendental equations

$$\tan k_{1z}d = -i\frac{\epsilon_1 k_z}{\epsilon k_{1z}}, \quad \text{for TM waves} \quad (A5a)$$

$$\tan k_{1z}d = -i\frac{\mu k_{1z}}{\mu_1 k_z}, \quad \text{for TE waves.} \quad (A5b)$$

It can be shown that the above can only have solutions in a certain domain of the complex plane, and thus the nature of the waves due to the pole contributions can be predetermined. When d is small, there is no pole contribution for TE

waves, and for TM waves, there is at most one pole. The location of the pole, in the limit that $d \to 0$, is given by

$$k_{pp} \sim k + \frac{1}{2}(k^3 d^2/k_1^4)(k^2 - k_1^2)^2. \quad (A6)$$

Physically, this implies that when d is small, there is at most one guided mode for the TM waves that can be excited, and for the TE waves, there is no mode excited. This is true of the microstrip substrate since the dielectric layer is thin.

It can be shown easily that (A3) and (A4) are even functions of k_{1z}. Therefore, there is no branch point at $k_p = k_1$. When $|\rho' - \rho| \to \infty$ we can replace $H_0^{(1)}(k_p|\rho' - \rho|)$ by $(2/\pi k_p|\rho' - \rho|)^{1/2}e^{ik_p|\rho' - \rho|}$ in (A1) and (A2). Thus there is a stationary point at $k_{ps} = k \sin\theta$, where

$$\theta = \tan^{-1}(|\rho' - \rho|/z).$$

The locations of the singularities, the stationary point, and the steepest descent path passing through it are shown in Fig. 5.

The pole gives rise to a surface wave which decays rapidly from the surface since k_{pp} is pure imaginary. Thus when $|\rho' - \rho| \to \infty$ and $z \to \infty$, in other words, when we are in the far field, the dominant contribution to (A1) and (A2) comes from the stationary point. With the steepest-descent analysis, it can be shown that

$$I_1 \sim \frac{2}{i}[1 - R^{1M}(\theta)]\frac{e^{ik|r - \rho'|}}{|r - \rho'|}$$

$$\sim \frac{2}{i}[1 - R^{1M}(\theta)]\frac{e^{ikr - i\rho'}}{r}, \quad (A7)$$

$$I_2 \sim \frac{2}{i}[1 + R^{11}(\theta)]\frac{e^{ik|r - \rho'|}}{|r - \rho'|}$$

$$\sim \frac{2}{i}[1 + R^{11}(\theta)]\frac{e^{ikr - ik\rho'}}{r}. \quad (A8)$$

We can use the above to derive Eqs. (6)–(8).

APPENDIX B: EVALUATION OF THE E-FIELD FOR A CIRCULAR DISK ANTENNA

First we shall evaluate the E_ϕ component given by Eq. (8). It can be shown easily that Eq. (8) can be reduced to

$$E_\phi = -\frac{\omega\mu}{4\pi i}[1 + R^{11}(\theta)]\frac{e^{ikr}}{r}\int_0^a\int_0^{2\pi}\rho'\,d\rho'\,d\phi'\,[K_\phi\cos(\phi' - \phi) + K_\rho\sin(\phi' - \phi)]\exp[-ik\rho'\sin\theta\cos(\phi - \phi')]. \quad (B1)$$

Letting the integral part of the expression above be I_1, substituting with Eqs. (11a) and (11b) results in

$$I_1 = \int_0^a\int_0^{2\pi}\rho'\,d\rho'\,d\phi'\,i(\epsilon_1/\mu_1)^{1/2}E_0\left[\frac{n}{(\beta_{nm}/a)\rho'}J_n\left(\frac{\beta_{nm}}{a}\rho'\right)\sin n\phi'\cos(\phi' - \phi) - J_n'\left(\frac{\beta_{nm}}{a}\rho'\right)\cos n\phi'\sin(\phi' - \phi)\right]$$
$$\cdot \exp[-ik\rho'\sin\theta\cos(\phi - \phi')]. \quad (B2)$$

Using the fact that

$$J_n(x) = \frac{1}{2\pi}\int_0^{2\pi}d\phi\exp(-ix\cos\phi - in\phi + \frac{1}{2}in\pi),$$

and that $J_{-n}(x) = (-1)^nJ_n(x)$, it can be shown that

$$\int_0^{2\pi}\cos n\phi'\sin(\phi' - \phi)\exp[-ik\rho'\sin\theta\cos(\phi' - \phi)]\,d\phi' = n(-i)^{n+1}\frac{2\pi}{k\rho'\sin\theta}J_n(k\rho'\sin\theta)\sin n\phi \quad (B3)$$

and

$$\int_0^{2\pi}\sin n\phi'\cos(\phi' - \phi)\exp[-ik\rho'\sin\theta\cos(\phi' - \phi)]\,d\phi' = 2\pi(-i)^{n+1}J_n'(k\rho'\sin\theta)\sin n\phi. \quad (B4)$$

Therefore (B2) becomes

$$I_1 = i(\epsilon_1/\mu_1)^{1/2}E_0 n(-i)^{n+1} 2\pi \sin n\phi \int_0^a d\rho' \left(\frac{J_n[(\beta_{nm}/a)\rho']J_n'(k\rho'\sin\theta)}{(\beta_{nm}/a)} + \frac{J_n'[(\beta_{nm}/a)\rho']J_n(k\rho'\sin\theta)}{k\sin\theta} \right). \quad \text{(B5)}$$

Recognizing the integrand to be exact derivative, we have

$$I_1 = (\epsilon_1/\mu_1)^{1/2}E_0 n(-i)^{n+1} \frac{2\pi \sin n\phi}{(\beta_{nm}/a)k\sin\theta} J_n(\beta_{nm})J_n(ka\sin\theta),$$

or

$$E_\phi = -\omega\mu(\epsilon_1/\mu_1)^{1/2}\frac{e^{ikr}}{2r} n(-i)^{n+1} \frac{E_0 \sin n\phi}{(\beta_{nm}/a)k\sin\theta} J_n(\beta_{nm})J_n(ka\sin\theta)[1+R^{11}(\theta)].$$

Next, we shall evaluate the E_θ component which is derivable from Eqs. (6) and (7). Thus

$$E_\theta = \frac{ik^2\cos\theta}{4\pi\omega\epsilon}(1-R^{TM}(\theta))\frac{e^{ikr}}{r} \int_0^a \int_0^{2\pi} \rho' d\rho' d\phi' [K_\rho \cos(\phi-\phi')$$
$$+ K_A \sin(\phi-\phi')] \exp[-ik\rho'\sin\theta\cos(\phi-\phi')]. \quad \text{(B7)}$$

Letting the integral part of the above expression be I_2, and substituting with (11a) and (11b), we have

$$I_2 = \int_0^a \int_0^{2\pi} \rho' d\rho' d\phi' i(\epsilon_1/\mu_1)^{1/2}E_0 J_n'\left(\frac{\beta_{nm}}{a}\rho'\right)\cos n\phi' \cos(\phi-\phi') - \frac{an}{\beta_{nm}\rho'} J_n\left(\frac{\beta_{nm}}{a}\rho'\right)\sin n\phi' \sin(\phi-\phi')$$
$$\times \exp[-ik\rho'\sin\theta\cos(\phi-\phi')]. \quad \text{(B8)}$$

It can be shown that

$$\int_0^{2\pi} \cos n\phi' \cos(\phi-\phi')\exp[-ik\rho'\sin\theta\cos(\phi-\phi')] = -2\pi(-i)^{n+1}\cos n\phi J_n'(k\rho'\sin\theta), \quad \text{(B9)}$$

$$\int_0^{2\pi} \sin n\phi' \sin(\phi-\phi')\exp[-ik\rho'\sin\theta\cos(\phi-\phi')] = \frac{2\pi n(-i)^{n+1}}{k\rho'\sin\theta}\cos n\phi J_n(k\rho'\sin\theta). \quad \text{(B10)}$$

Therefore

$$I_2 = -i(\epsilon_1/\mu_1)^{1/2}E_0 2\pi(-i)^{n+1}\cos n\phi \int_0^a d\rho'\left[\rho' J_n'\left(\frac{\beta_{nm}}{a}\rho'\right)J_n'(k\rho'\sin\theta) + \frac{n^2 J_n(k\rho'\sin\theta)J_n[(\beta_{nm}/a)\rho']}{(\beta_{nm}/a)k\rho'\sin\theta}\right]. \quad \text{(B11)}$$

It can be shown that

$$\rho' J_n'\left(\frac{\beta_{nm}}{a}\rho'\right)J_n'(k\rho'\sin\theta) + \frac{n^2 J_n[(\beta_{nm}/a)\rho']J_n(k\rho'\sin\theta)}{(\beta_{nm}/a)k\rho'\sin\theta}$$
$$= \left[\left(\frac{\beta_{nm}}{a}\right)^2 - k^2\sin^2\theta\right]^{-1} \frac{\partial}{\partial\rho'}\left[\frac{\beta_{nm}}{a}\rho' J_n\left(\frac{\beta_{nm}}{a}\rho'\right)J_n'(k\sin\theta\rho') - k\sin\theta\rho' J_n'\left(\frac{\beta_{nm}}{a}\rho'\right)J_n(k\sin\theta\rho')\right]. \quad \text{(B12)}$$

As such

$$I_2 = (\epsilon_1/\mu_1)^{1/2} \frac{(\beta_{nm}/a)E_0}{[(\beta_{nm}/a)^2 - k^2\sin^2\theta]} 2\pi(-i)^{n+2}\cos n\phi\, aJ_n(\beta_{nm})J_n'(k\sin\theta a) \quad \text{(B13)}$$

and

$$E_\theta = (\epsilon_1/\mu_1)^{1/2}\omega\mu\frac{e^{ikr}}{2r}(-i)^{n+1}E_0\cos\theta\cos n\phi \frac{(\beta_{nm}/a)}{(\beta_{nm}/a)^2 - k^2\sin^2\theta}[aJ_n(\beta_{nm})J_n'(ka\sin\theta)][1-R^{TM}(\theta)]. \quad \text{(B14)}$$

[1] R. Wait, Can. J. Phys. **29**, 577–592 (1951).
D. B. Brick, Proc. IEEE **102**, C, 104–121 (1955).
L. M. Brekhovskikh, *Waves in Layered Media* (Academic, New York, 1960).
J. A. Kong, Geophysics **37**, 985–996 (1972).
J. A. Kong, *Theory of Electromagnetic Waves* (Wiley, New York, 1975).
S. A. Long, L. C. Shen, and P. B. Morel, Proc. IEEE **125**, 925–928 (1978).
R. E. Collin, *Foundation of Microwave Engineering* (McGraw-Hill, New York, 1966).

[8] K. Kurokawa, IRE Trans. Microwave Theory and Tech. **MTT-6**, 178–187 (1958).
M. D. Walton, M.S. Thesis, University of Houston, Texas, 1976.
J. Watkins, Electron. Lett. **5**, 524–525, (1969).
W. C. Chew and J. A. Kong, J. Math. Phys. (to be published)
W. C. Chew and J. A. Kong, J. Math. Phys. **21**, No. 3, 582 (1980).

The Elliptical Microstrip Antenna with

Circular Polarization

L. C. Shen
Department of Electrical Engineering
University of Houston
Houston, Texas 77004

Abstract

Theoretical analysis of an elliptical microstrip antenna is presented. It is shown that radiation from this antenna is left-hand or right-hand circularly polarized in a narrow frequency band when the eccentricity of the ellipse is small. The theoretical result agrees with the experimental data.

1. Introduction

Microstrip antennas of circular or rectangular shapes usually radiate
linearly polarized waves. In many practical applications circular polari-
zation is required. Circular polarization may be obtained by using multiple
feeds [1] or by altering the shape of a rectangular microstrip antenna [2].
It is also known that a simple microstrip antenna, namely, an elliptical patch
on a microwave printed-circuit board, can be made to radiate circularly polar-
ized waves [3]. Such an antenna requires only one feed and its geometrical
shape is simple enough to permit rigorous theoretical analysis to be carried
out in a standard coordinate system. In the present study, the radiated field
of an elliptical microstrip antenna is obtained in terms of tabulated functions.
The effects of the fringe field at the edge of the elliptical patch and those of
the dielectric substrate are taken into account in the calculation.

2. The Elliptic Coordinates

An elliptical microstrip antenna is shown in Fig. 1 in which the parameters
a, b, c and d are also defined. The elliptical conducting patch may be obtained
by applying photolithographic techniques to a microwave printed-circuit board.
The antenna may be driven on the edge at ϕ_0 degree from the semi-major axis by
a coaxial line through the dielectric substrate (as shown in Fig. 1) or by a
microstrip line.

Elliptical coordinates of u and v are used in substitution of x-y coordi-
nates while the z axis remains unaffected. For an ellipse of semi-major axis
a and semi-minor axis b, the foci are at x = ±c where

$$c = (a^2 - b^2)^{1/2} . \tag{1}$$

The x-y coordinates are related to the u-v coordinates by the following formulas:

$$x = c \cosh u \cos v \tag{2a}$$

$$y = c \sinh u \sin v . \tag{2b}$$

The ellipse is defined by

$$u = u_0 = \ln(\frac{a+b}{c}) , \tag{3}$$

and the driving-point is at the elliptical coordinates $(u = u_0, v = v_0)$ where

$$v_0 = \tan^{-1}(\frac{\tan \phi_0}{\tanh u_0}) . \tag{4}$$

The eccentricity of the ellipse is defined as

$$e_c = \frac{c}{a} \tag{5}$$

Assuming that the thickness of the dielectric substrate is much smaller than a wavelength in the dielectric so that fields in the dielectric do not vary with respect to z, the Maxwell's equations reduce to the following set of equations:

$$\frac{\partial^2 E_z}{\partial u^2} + \frac{\partial^2 E_z}{\partial v^2} + k_1^2 c^2 (\cosh^2 u - \cos^2 v) E_z = 0 \tag{6}$$

$$H_u = \frac{j}{\omega\mu c \sqrt{\cosh^2 u - \cos^2 v}} \frac{\partial E_z}{\partial v} \tag{7}$$

$$H_v = \frac{-j}{\omega\mu c \sqrt{\cosh^2 u - \cos^2 v}} \frac{\partial E_z}{\partial u} \tag{8}$$

$$H_z = 0, \quad E_u = 0, \text{ and } E_v = 0,$$

and

$$k_1 = \omega\sqrt{\mu_0 \epsilon_1} . \tag{9}$$

Throughout the analysis the time factor $e^{j\omega t}$ is used; the magnetic permeability μ of the dielectric is equal to that of the air, that is, $\mu = \mu_0$; and the permittivity of the dielectric and that of air are denoted ϵ_1 and ϵ_0, respectively.

3. Mathieu Functions

Solutions to the partial differential Equation (6) may be expressed in terms of Mathieu functions $S_{om}(C,\cos v)$ and $S_{em}(C,\cos v)$ and related radial functions $J_{om}(C,\cosh u)$ and $J_{em}(C,\cosh u)$ [4].

$$E_z = \sum_{m=0}^{\infty} [A_m S_{om}(C,\cos v) J_{om}(C,\cosh u)$$

$$+ B_m S_{em}(C,\cos v) J_{em}(C,\cosh u)] \tag{10}$$

where $C = k_1 c$.

In practical applications, the excitation of the $m = 1$ mode is favored since

it has the lowest resonant frequency and its radiation is mainly in the z direction. Therefore and from hereafter, only two terms in (10) corresponding to the m = 1 mode will be retained.

Since the electric field has a z component only, the boundary condition on the upper conducting patch and on the lower conducting ground plate is automatically satisfied. The only boundary condition to be imposed is on the elliptical edge defined by $u = u_0$:

$$-H_v = K_z + E_z y_s \quad (\text{at } u = u_0) \ . \tag{11}$$

In the above equation, H_v can be calculated from (8) and (10); E_z is given by (10); K_z is the current maintained by the transmission line at the driving point (u_0, v_0):

$$K_z = \frac{I_0}{C\sqrt{\cosh^2 u_0 - \cos^2 v_0}} \delta(v - v_0) \tag{12}$$

where I_0 is the total current at the driving point, and y_s is the surface admittance as seen by the elliptical cavity bounded by $u \leq u_0$ and $-d \leq z \leq 0$. The surface admittance takes into account the effect of radiation and the fringe field. Its value will be given later.

Multiplying S_{o1} on both sides of (11) and integrating over v from 0 to 2π yields the following:

$$A_1 = \frac{-j\omega\mu \ I_0 S_{o1}(C, \cos v_0)/M_1^0}{\dfrac{\partial J_{o1}}{\partial u}\bigg|_{u_0} + j y_s \omega\mu C\sqrt{\cosh^2 u_0 - \cos^2 v_0} \ J_{o1}(C, \cosh u_0)} \tag{13}$$

B_1 may be obtained by a similar procedure:

$$B_1 = \frac{-j\omega\mu\ I_0 S_{e1}(C,\cos v_0)/M_1^e}{\frac{\partial J_{e1}}{\partial u}\Big|_{u_0} + jy_s\omega\mu C\sqrt{\cosh^2 u_0 - \cos^2 v_0}\ J_{e1}(C,\cosh u_0)} \tag{14}$$

where $M_1^o = \int_0^{2\pi} S_{o1}^2\ dv$ and $M_1^e = \int_0^{2\pi} S_{e1}^2\ dv$.

4.   Approximate Formulas

Experimental data [3] showed that the elliptical antenna would produce circular polarization only if the eccentricity was small. Difference between a and b was of the order of a few percent. That is, the ellipse should almost be a circle. For small eccentricity, $C = k_1 c < 1$, approximate formulas for the Mathieu functions are available [4]:

$$S_{o1}(C,\cos v) = (1+3C^2/32)\sin v - (C^2/32)\sin 3v \tag{15}$$

$$J_{o1}(C,\cosh u) = \sqrt{\frac{\pi}{2}}\ \frac{1}{(1+C^2/8)}\ [(1+3C^2/32)J_1(C\ \sinh u)$$
$$- (C^2/32)J_3(C\ \sinh u)] \tag{16}$$

$$S_{e1}(C,\cos v) = (1+C^2/32)\cos v - (C^2/32)\cos 3v \tag{17}$$

$$J_{e1}(C,\cosh u) = \sqrt{\frac{\pi}{2}}\ [(1+C^2/32)J_1(C\ \cosh u)$$
$$+ (C^2/32)J_3(C\ \cosh u)] \tag{18}$$

$$M_1^e = \pi(1 + C^2/16) \tag{19}$$

$$M_1^o = \pi(1 + 3C^2/16) \tag{20}$$

In (16) and (18), J_1 and J_3 are Bessel functions of order 1 and 3, respectively. Again, since the ellipse is almost a circle with $0.97 < b/a < 1$

the admittance surface y_s of a circle can be used [5]:

$$y_s = g_s + j\, b_s \, , \tag{21}$$

$$g_s = \frac{d}{2a\zeta_0}\, [(k_0 a)^2 I_1 + I_2] \tag{22}$$

$$I_1 = \int_0^\pi [J_1'(k_0 a\, \sin\theta)]^2 \sin\theta\; d\theta \, , \tag{23}$$

$$I_2 = \int_0^\pi \frac{\cos^2\theta}{\sin\theta}\, [J_1(k_0 a\, \sin\theta)]^2\; d\theta, \tag{24}$$

$$b_s = J_1'(w)/[\zeta_1 J_1(w)] \, , \tag{25}$$

$$w = 1.841/(1+\Lambda)^{1/2} \, , \tag{26}$$

$$\Delta = \frac{2d\epsilon_0}{\pi\epsilon_1 a}\, [\ell n(\frac{a}{2d}) + 1.41\, \frac{\epsilon_1}{\epsilon_0} + 1.77$$

$$+ \frac{d}{a}\, (0.268\, \frac{\epsilon_1}{\epsilon_0} + 1.65)] \tag{27}$$

$$\zeta_0 = (\mu_0/\epsilon_0)^{1/2} \tag{28}$$

$$\zeta_1 = (\mu_0/\epsilon_1)^{1/2} \, . \tag{29}$$

The surface conductance g_s is determined by the power radiated through the opening of the cavity, and the surface susceptance b_s is determined by the fringe field which increases the capacitance by a factor of $(1+\Delta)$. The formula for Δ stated here is due to Chew and Kong [6] who obtained this formula which is more accurate than the one used in [5].

5. Radiated Field

The internal fields of the elliptical microstrip antenna are completely determined in terms of the approximate formulas presented in the preceding

section. The radiated electric field $\overline{E}^r$ can then be calculated from E_z which sets up an equivalent magnetic current at $u = u_0$, $0 < v < 2\pi$:

$$\overline{E}^r = \nabla \times \overline{F} \tag{30}$$

$$\overline{F} = -\int_0^{2\pi} h_v \, dv' \int_{-d}^{0} dz' \, G \, E_z \, \hat{v}' \tag{31}$$

where $h_v = C\sqrt{\cosh^2 u_0 - \cos^2 v_0}$ and G is the free-space Green's function. By using the free-space Green's function the effect on the radiation field of the dielectric layer in the external region ($u > u_0$) is neglected. However, according to an analysis by Kong [7], the effect can be taken into account by introducing a factor to the final result. This will be done later in the present analysis.

Substituting (10) in (31), noting that

$$h_v \, \hat{v}' = -a \, \sin v \, \hat{x} + b \, \cos v \, \hat{y} , \tag{32}$$

and after rather tedious manipulations of the integral, the following re-sults are derived:

$$E_\theta = \frac{e^{-jk_0 r}}{4\pi r} \left\{ \frac{k_1^2}{k_1^2 - k_0^2 \sin^2\theta} \cos\theta [1 - R^{TM}(\theta)] \right\} (I_x \sin\phi - I_y \cos\phi) \tag{33}$$

$$E_\phi = \frac{e^{-jk_0 r}}{4\pi r} [1 + R^{TE}(\theta)](I_x \cos\phi + I_y \sin\phi) \tag{34}$$

where k_0 and k_1 are wavenumbers in free space and in the dielectric, re-spectively. Spherical coordinates r, θ, ϕ are used. Furthermore,

$$1-R^{TM}(\theta) = \frac{1-e^{-j2k_{1z}d}}{1+R_{01}^{TM}e^{-j2k_{1z}d}} (1-R_{01}^{TM}) \ , \tag{35}$$

$$1+R^{TE}(\theta) = \frac{1-e^{-j2k_{1z}d}}{1-R_{01}^{TE}e^{-jk_{1z}d}} (1+R_{01}^{TE}) \ , \tag{36}$$

$$R_{01}^{TM} = \frac{k_{0z}-k_{1z}}{k_{0z}+k_{1z}} \ , \tag{37}$$

$$R_{01}^{TE} = \frac{k_{0z}k_1^2-k_0^2k_{1z}}{k_{0z}k_1^2+k_0^2k_{1z}} \ , \tag{38}$$

$$k_{0z} = k_0\cos\theta \ , \tag{39}$$

$$k_{1z} = (k_1^2-k_0^2 \sin^2\theta)^{1/2} \tag{40}$$

$$I_x = -\pi a\{A'[J_0-J_2\cos2\alpha + \frac{C^2}{32} (3J_0-4J_2\cos2\alpha+J_4\cos4\alpha)]$$
$$- B'[J_2\sin2\alpha - \frac{C^2}{32} J_4\sin4\alpha]\} \tag{41}$$

$$I_y = \pi b\{A'[-J_2\sin2\alpha + \frac{C^2}{32} (-2J_2\sin2\alpha+J_4\sin4\alpha)]$$
$$+ B'[J_0+J_2\cos2\alpha + \frac{C^2}{32} (J_0-J_4\cos4\alpha)]\} \tag{42}$$

$$A' = A_1 J_{o1}(C, \cosh u_0) \ . \tag{43}$$

$$B' = B_1 J_{e1}(C, \cosh u_0) \ , \tag{44}$$

$$\alpha = \tan^{-1}(\frac{a \cos\phi}{b \sin\phi}), \tag{45}$$

and J_0, J_2, and J_4 are Bessel functions of under 0, 2, and 4, respectively

with argument Q where

$$Q = k_0 \sin\theta (a^2 \cos^2\phi + b^2 \sin^2\phi)^{1/2} \tag{46}$$

In (33-34) factors have been introduced to take into account the presence of the dielectric layer.

6. Results and Discussion

The radiated electric fields are given in (33) and (34) are in terms of simple trigonometric functions and Bessel functions for which efficient computer programs are readily available. In Fig. 2 the amplitude and phase of E_x and E_y on the z-axis (which is the direction of maximum radiation) are plotted as functions of frequency, with the position of the driving point as a variable parameter. It is seen that optimum circular polarization can be obtained when the driving point is placed at 45° to the major axis with frequency equal to 2.79 GHz. The effect of changing the position of the driving point is to change the relative amplitudes of the x directed and the y-direction electric fields. Moving the driving point toward the major axis enhances the excitation of current flowing parallel to the major axis and thus results in greater amplitude for E_x. It is also seen that the phase is not a sensitive function of ϕ_0. The elliptical microstrip antenna for which Fig. 2 is produced has b/a = 0.98. In Fig. 3, the fields of a microstrip antenna of b/a = 0.96 are calculated. It is seen that although E_x is equal to E_y in amplitude at f = 2.82 GHz, the phase difference is greater than 90° so that the quality of circular polarization is not as good as that shown in Fig. 2. Note that in Fig. 2 as the frequency

is changed from the optimum frequency, not only do the relative ampliudes of E_x and E_y change but also the relative phase angles deviate from the ideal 90° value. Polarization ellipses on the z axis are shown in Fig. 4 as functions of the operating frequency. Arrows indicate direction of rotation of E field at a fixed point in the z axis. Thus in Fig. 4 all fields are left-hand elliptically polarized.

Radiation patterns of an elliptical antenna with b/a = 0.98 operated at the optimum frequency for circular polarization are shown in Figs. 5a and 5b. It is seen that quality of circular polarized is quite good for θ less than 45°. The polarization ellipses are shown in Fig. 6 for various θ angles.

Based on extensive experimental data, Yu [3] discovered the following characteristics of the elliptical microstrip antenna.

(a) "Generally, the radiation associated with the elliptical antenna element is elliptically polarized, but is circularly polarized when the antenna element is coupled through a feed point on a radial line of the elliptical lamina which is oriented at a 45° azimuthal angle relative to a semimajor axis of the ellipse. If the radial line on which the feed point is located is rotated 45° counter clockwise relative to a semimajor axis of the ellipse, the polarization of the radiation communicable by the antenna element will be left-circularly polarized. If the radial line on which the feed point is located is oriented at an angle of 45° clockwise relative to a semimajor axis of the ellipse, the polarization of the radiation in question will be right-circularly polarized". These statements are in agreement with the present

theory, as shown in Figs. 4 and 6. It is also noted that if ϕ_0 is changed to $\pi-\phi_0$, and ϕ to $\pi-\phi$ in all preceding formulas, then E_θ will be unchanged while E_ϕ is changed to $-E_\phi$, resulting in right-hand elliptically polarized radiation.

(b) To achieve an operating frequency f, the semimajor axis a of the ellipse is given by the equation $a = p/f\sqrt{\mu\epsilon_1}$, where p is an empirical constant ranging from 0.27 to 0.29. According to the present theory, using parameters in Figs. 2, 5, and 6, p is found to be equal to 0.275 which agrees very well with the empirical value.

(c) "It has been found that the desired circularly polarized radiation communicability may best be achieved by limiting the eccentricity of the ellipse to a range of 10 to 20%." For b/a = 1.84/1.88, the eccentricity is equal to 20.5%. Present theoretical results show that good circular polarization is obtained [Fig. 4(a)]. For b/a = 1.80/1.88, the eccentricity is equal to 28.9%. Present theory shows that quality of circular polarization is not very good, as seen from Fig. 4(b).

7. Conclusion

Currents, internal fields and radiated fields of an elliptical micro-strip antenna have been expressed in terms of Mathieu functions which may be expressed in terms of Bessel functions when the eccentricity of the ellipse is small. Left-hand or right-hand circular polarization can be obtained in a narrow frequency band for an elliptical microstrip antenna

of small eccentricity. Only one feed is needed to excite the circularly polarized antenna. All formulas are in terms of functions that can easily be programmed on small computers to facilitate the design of such an antenna for practical applications. Theoretical results are in good agreement with available experimental data.

8. Acknowledgment

9. References

1. G. G. Sanford, "Conformal microstrip phased array for aircraft tests with ATS-6," IEEE Trans. Antennas Propagat., Vol. AP-26, No. 5, pp. 642-646, 1978.

2. W. F. Richards, Y. T. Lo, and P. Simon, "Design and theory of circularly polarized microstrip antennas," 1979 IEEE AP-S International Symposium Digest, pp. 117-120.

3. I. P. Yu, "Low profile circularly polarized antenna," NASA Report N78-15332, 1978.

4. P. M. Morse and H. Feshbach, Methods of Theoretical Physics, p. 503 and p. 1407, McGraw-Hill, New York, 1953.

5. L. C. Shen, "Analysis of a circular-disc printed-circuit antenna," Proceedings of IEE (London), Vol. 126, No. 12, pp. 1220-1222.

6. W. C. Chew and J. A. Kong, "Effects of fringing fields on the capacitance of circular microstrip disk," To be published by IEEE Trans. Microwave Theory and Techniques.

7. J. A. Kong, Theory of Electromagnetic Waves, John-Wiley & Sons, Inc., New York, N. Y., 1975.

Figure Legends

Fig. 1   An elliptical microstrip antenna and the elliptical coordinates.

Fig. 2   Amplitudes and phases of E_x and E_y on the z axis of an elliptical microstrip antenna with a = 1.88 cm, b = 1.84 cm, d = 0.16 cm, ϵ_1 = 2.47 ϵ_0, driven at ϕ_0 with I_0 =1amp.

Fig. 3   Amplitudes and phases of E_x and E_y on the z axis of an elliptical microstrip antenna with a = 1.88 cm, b = 1.80 cm, d = 0.16 cm, ϵ_1 = 2.47 ϵ_0, driven at ϕ_0 with I_0 = 1 amp.

Fig. 4   Polarization ellipses on the z axis as functions of frequency (a) for elliptical antenna with b/a = 1.84/1.88 (b) for elliptical antenna with b/a = 1.80/1.88. Other parameters are same as those given in the legend of Fig. 2. Arrows indicate direction of rotation of the electric field. Antennas are driven at ϕ_0 = 45°, resulting in left-hand circular polarization.

Fig. 5   Radiation patterns of an elliptical microstrip antenna with parameters given in the legend of Fig. 2. Driving-point is at ϕ_0 = 45° (a) ϕ = 0 and π plane (b) ϕ = $\pi/2$ and $3\pi/2$ plane f = 2.79 GHz.

Fig. 6   Polarization ellipses as functions of θ produced by an elliptical microstrip antenna with parameters given in the legend of Fig. 2, driven at ϕ = 45°, with f = 2.79 GHz (a) on the ϕ = 0 plane (b) on the ϕ = 90° plane.
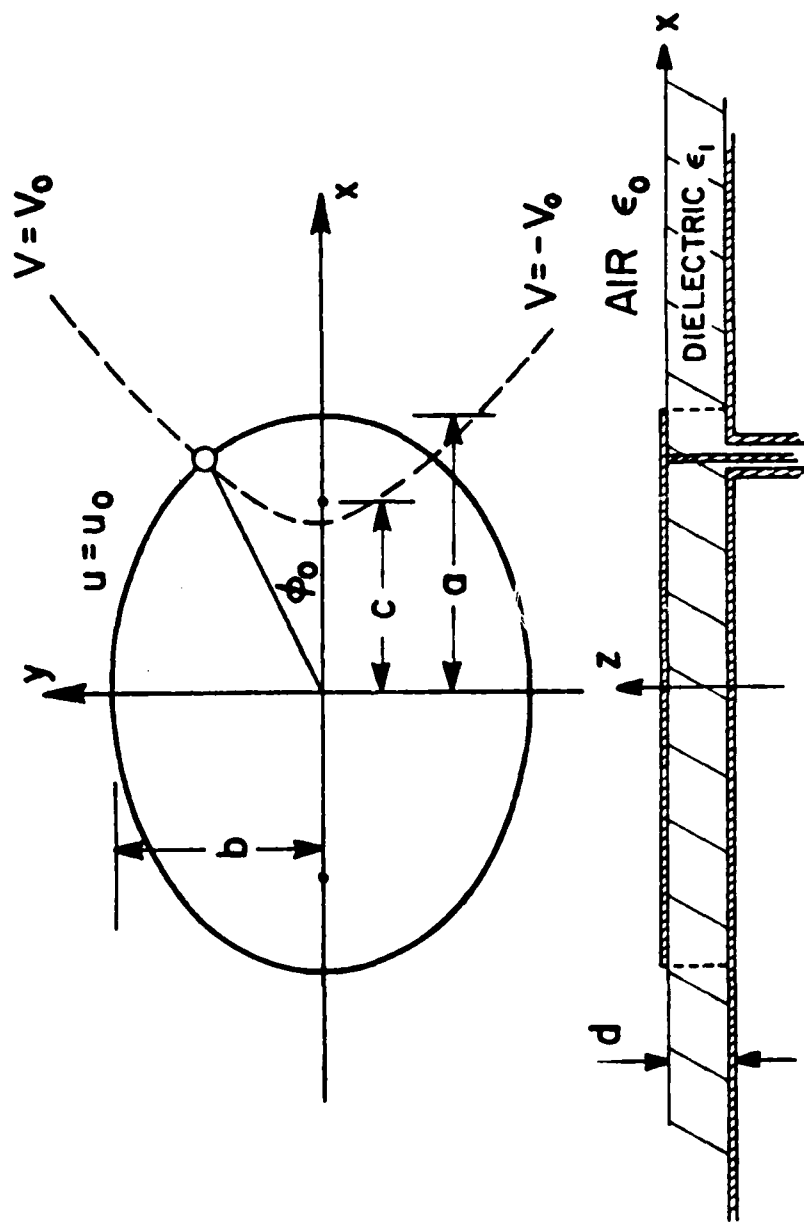
Figure 1

Figure 2
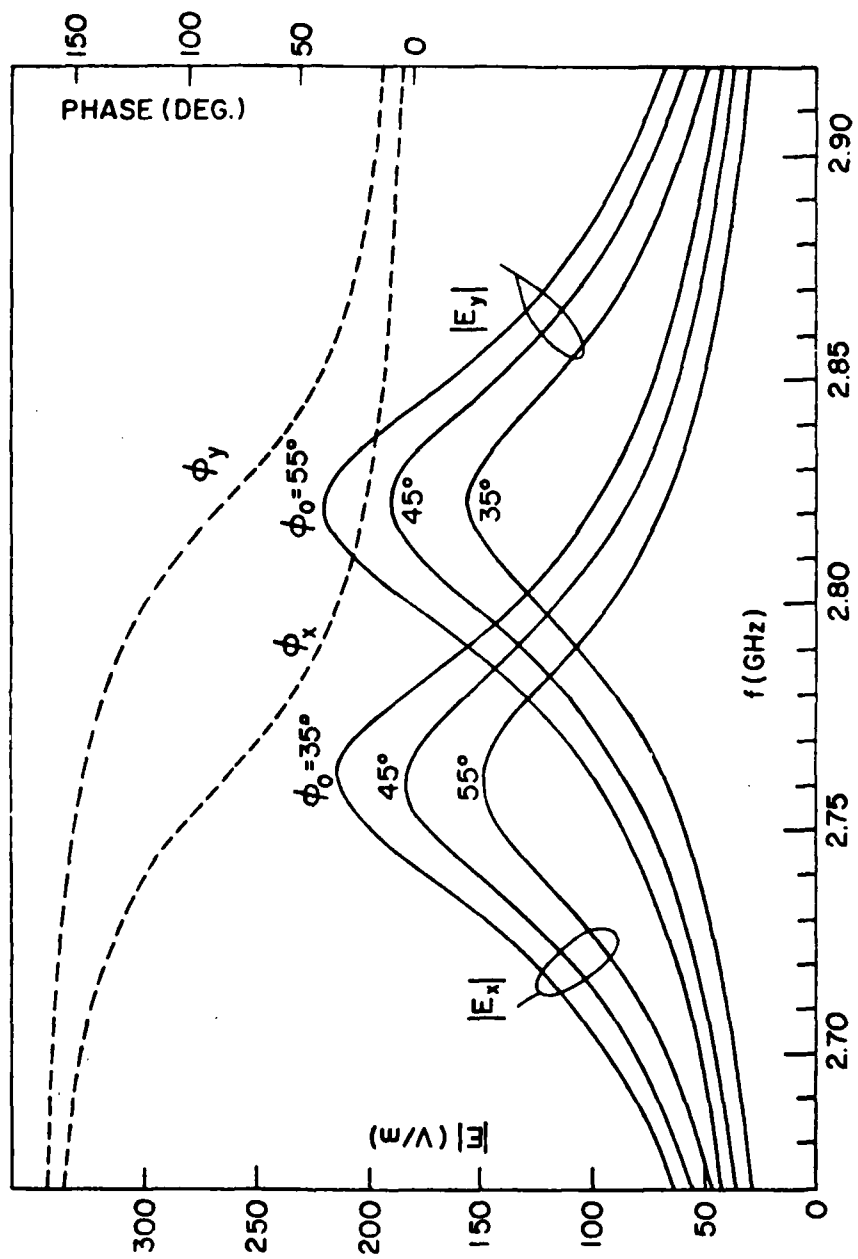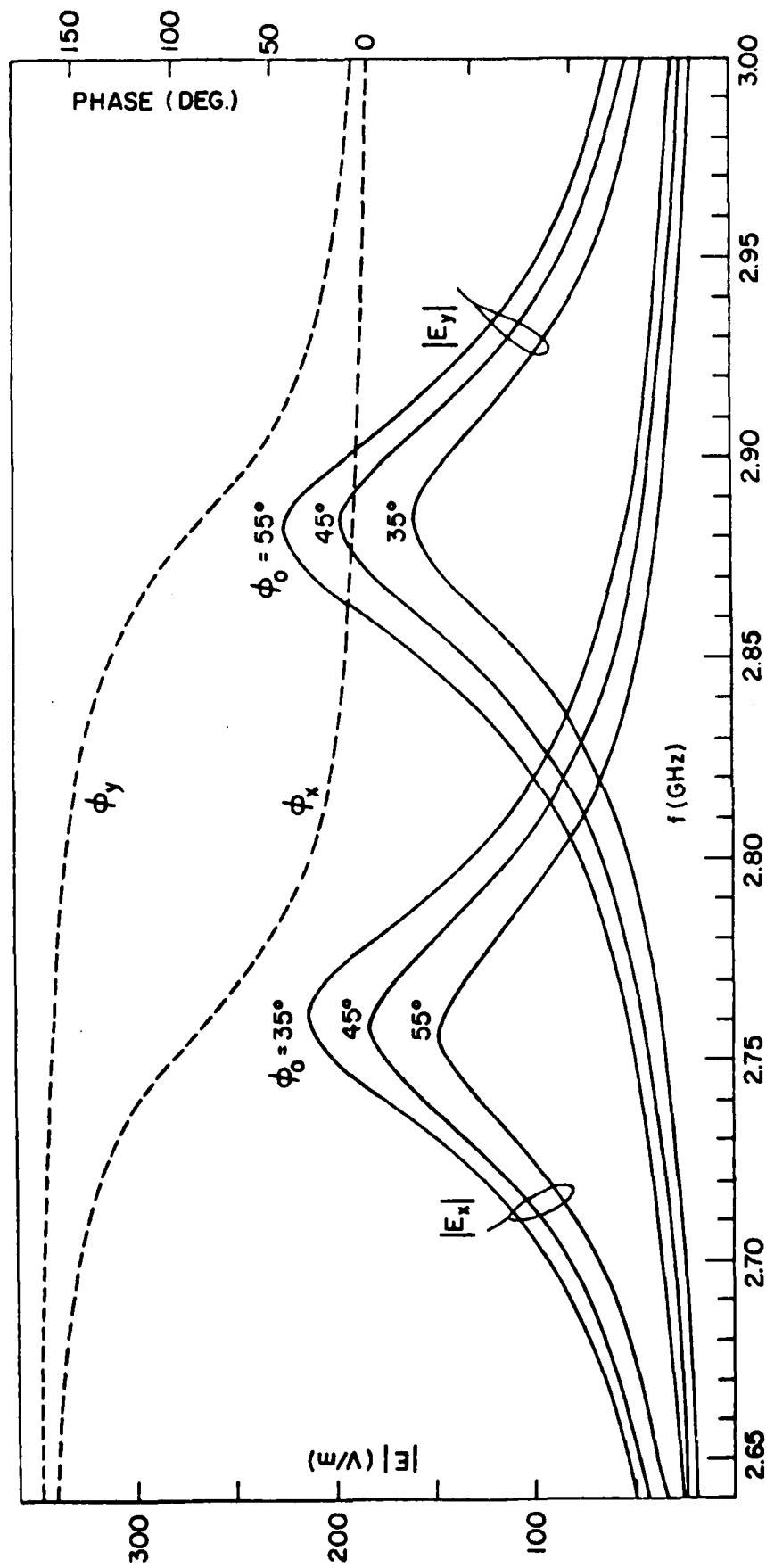
Figure 3
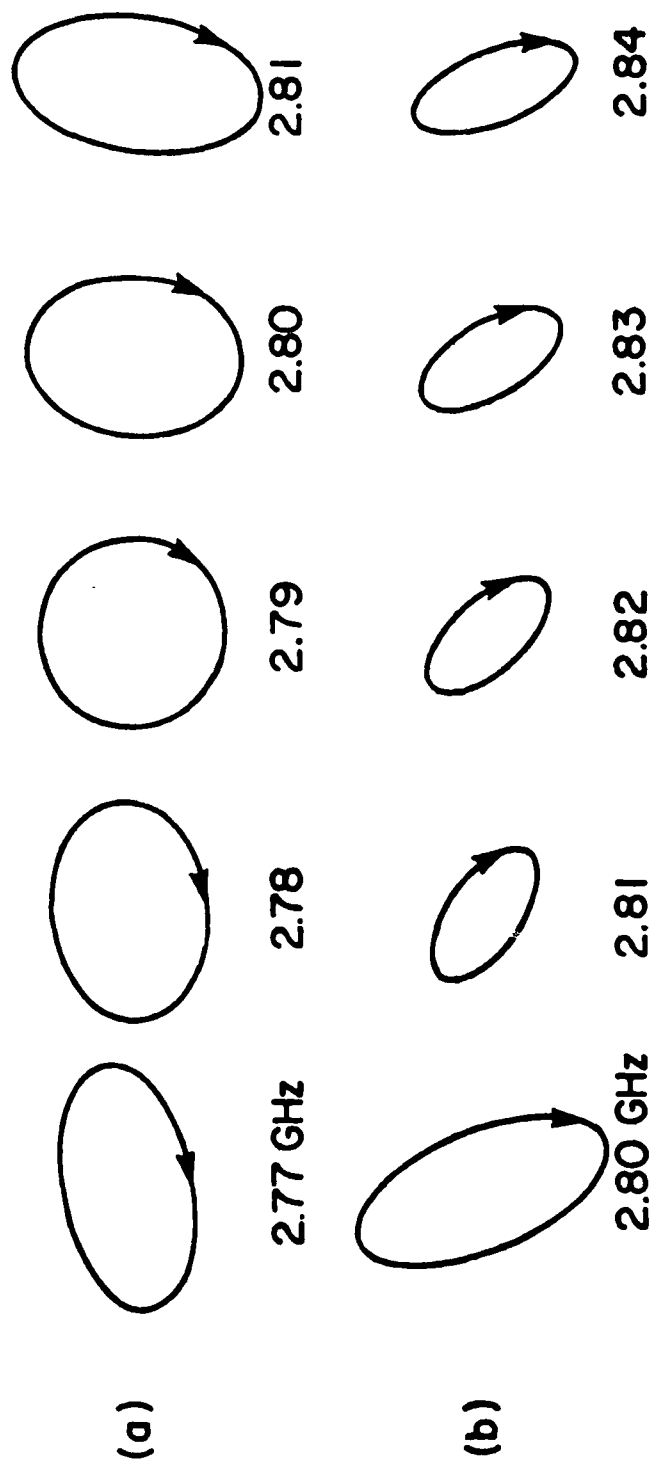
2.77 GHz   2.78   2.79   2.80   2.81   (a)

2.80 GHz   2.81   2.82   2.83   2.84   (b)
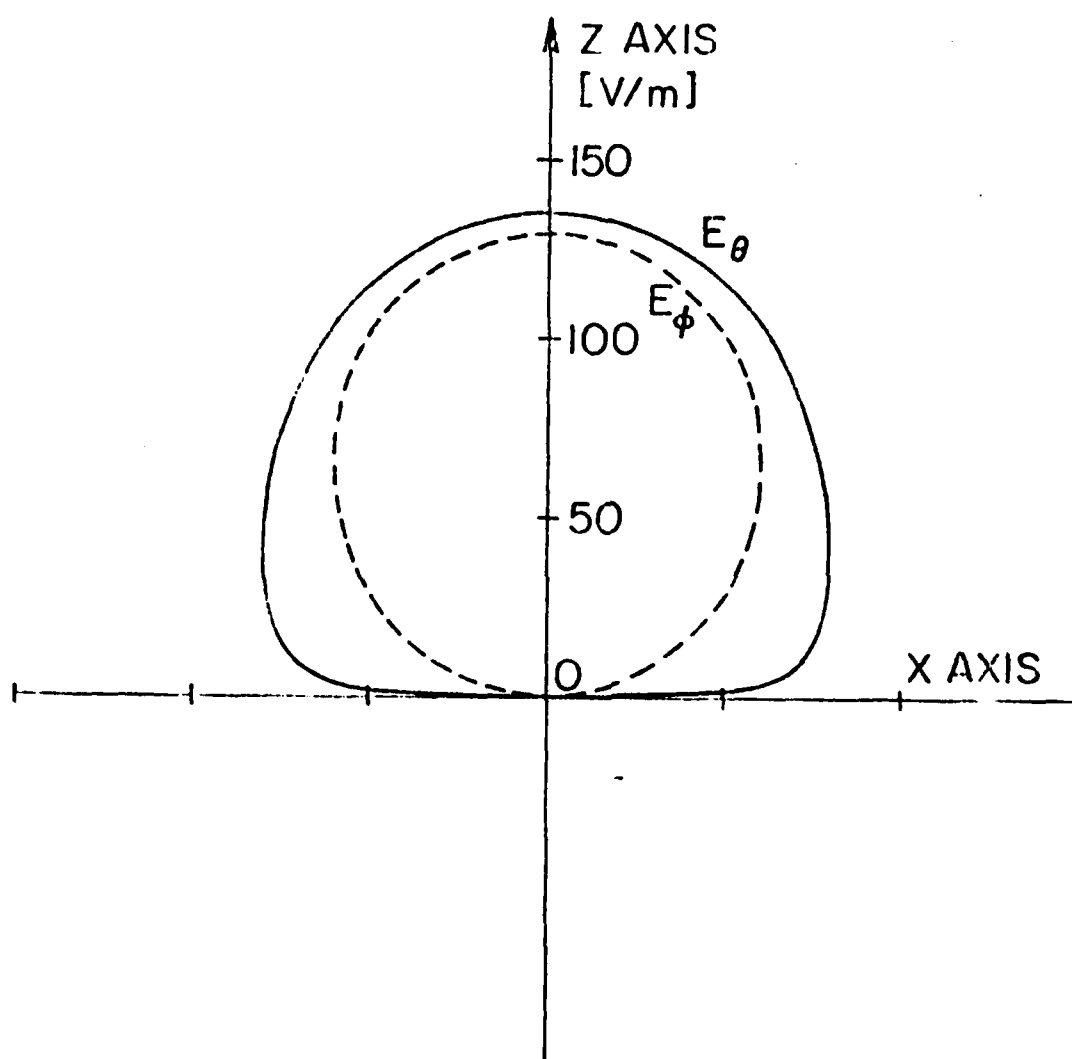
Figure 4

Figure 5a

(A)

(B)

θ = 0°

15°

30°

45°

60°

75°
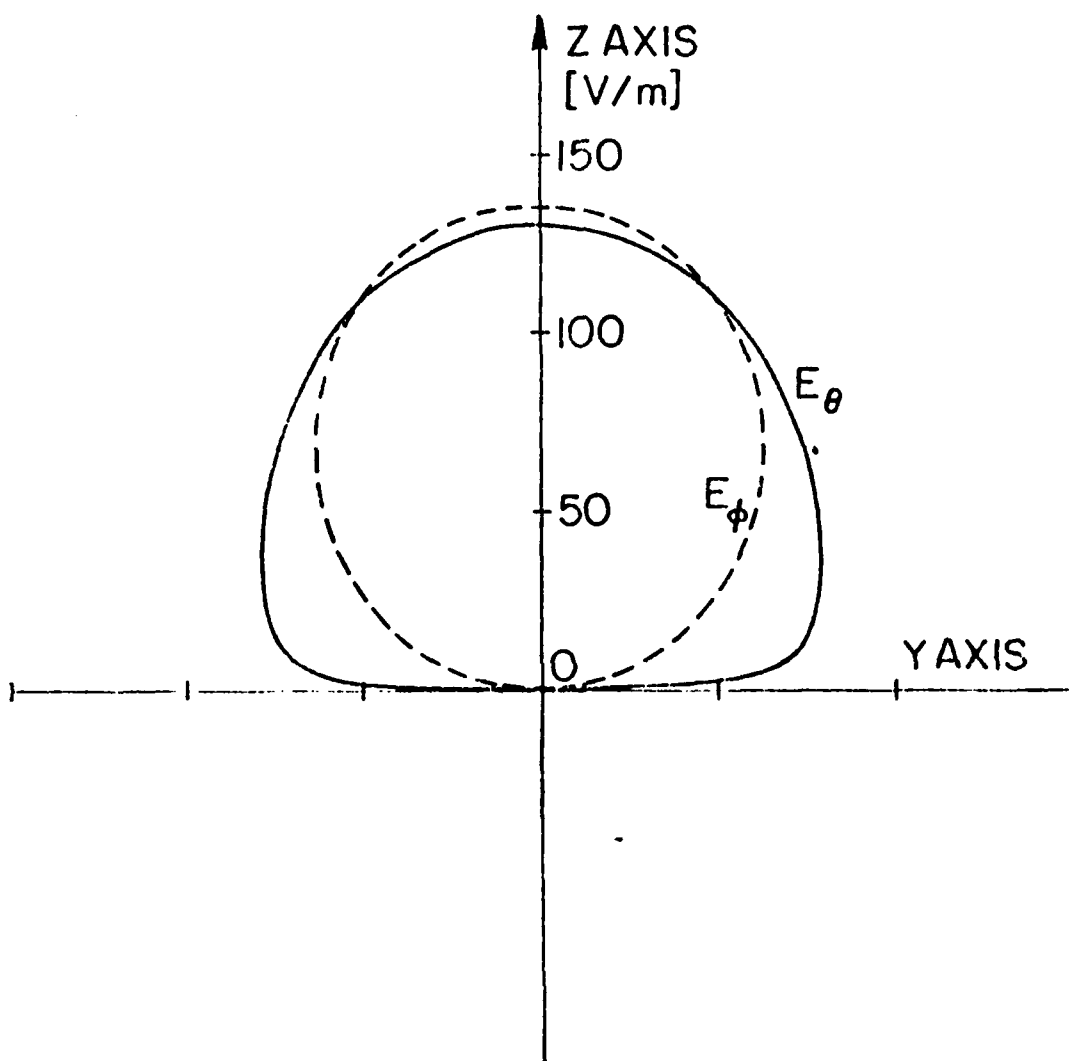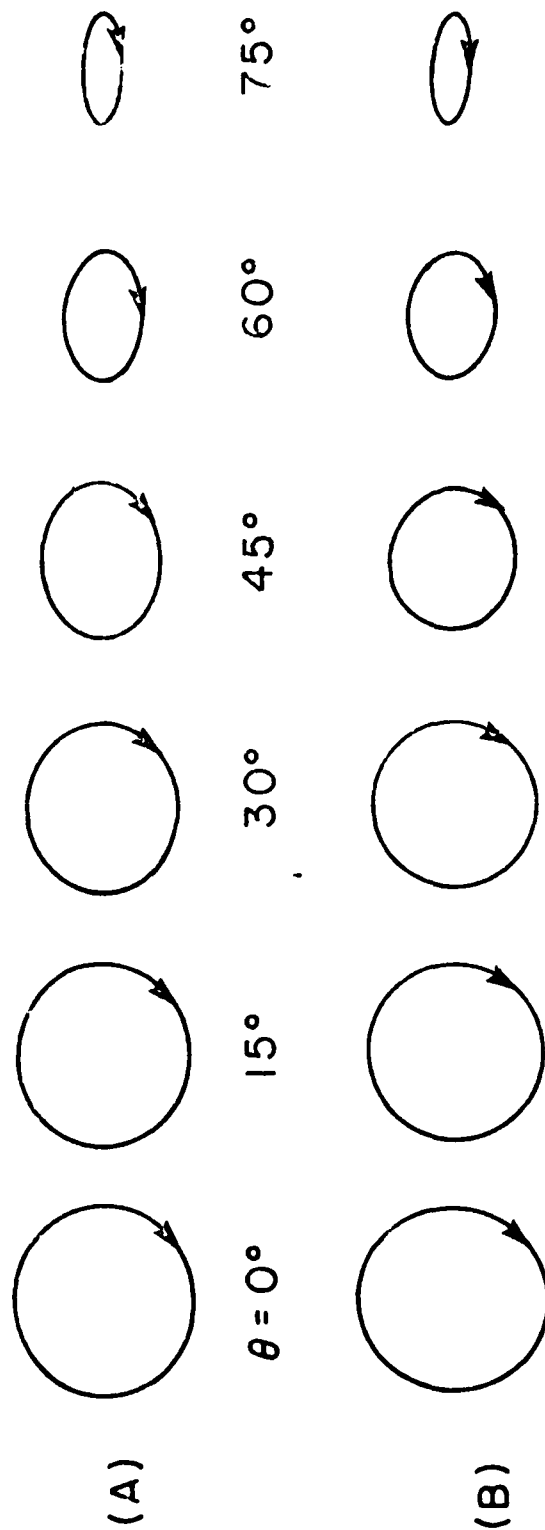
An Experimental Study of the Circular-Polarized,

Elliptical, Printed-Circuit Antenna

Stuart A. Long and Liang C. Shen
Department of Electrical Engineering
University of Houston
Houston, Texas   77004

Daniel H. Schaubert, and Frederick G. Farrar
Harry Diamond Laboratories
U.S. Army ERADCOM
Adelphi, Md   20783

Abstract

Elliptical shaped printed-circuit antennas were fabricated with varying eccentricities and their impedance and radiation patterns were measured. Special attention was devoted to investigating the design criteria which produced the best circular polarization.

E-1

I. Introduction

Over the past several years the printed-circuit antenna has proven to
be an efficient and effective radiator. In its simplest configuration,
whether rectangular or circular, it can be designed to produce a broad
beamwidth, linearly polarized radiation pattern with its maximum in the
direction normal to the plane of the antenna. The most direct approach
to provide circular polarization from such an antenna is to use two feeds
located geometrically 90 degrees apart and with a relative phase shift of
90°. This configuration excites two orthogonal modes each of which pro-
vides a linearly polarized wave at right angles to each other and shifted
in phase by 90°.

Several methods have been proposed to provide the desired circular
polarization without the additional complexities inherent in the dual feed
and phase-shifter radiator. The pentagon [1], corner-fed rectangle [2],
and the 45° slot [3] variations have all been designed for this purpose.
Recently Shen [4] has shown that circular polarization could also be
expected from a slightly elliptical radiator fed along a line 45° from its
major axis. Similar behavior had been seen experimentally by Yu [5] earlier
but never developed.

In this paper, a careful experimental study is carried out to investi-
gate the behavior of the radiated fields and the impedance of the ellipti-
cal radiator as a function of frequency, eccentricity, and dielectric thick-
ness. The results are then compared with the theoretical predictions of
Shen [4].

1

II.   Experimental Impedance Measurements

To investigate the properties of the elliptical printed-circuit antenna a set of ellipses with varying eccentricities were etched on two different thicknesses of printed-circuit board. The slightly elliptical discs shown in Figure 1 varied from a b/a ratio of 1.00 (that of a circle) to b/a = 0.96. The major radius remained constant at 4 cm while the minor radius was progressively reduced to about 3.84 cm. Five different ellipses were etched on both 0.3175 cm (~1/8") and 0.1575 cm (~1/16") thick teflon-fiberglass microwave printed-circuit board.

The impedance of each antenna was measured as a function of frequency from 1 to 2 GHz using an automatic network analyzer. An illustrative example of one of these swept frequency measurements is shown in Figure 2 in Smith chart format for the case of d = .3175 cm and b/a = .976. While no attempt was made to match the antennas to the characteristic impedance of the 50 ohm line, this could be accomplished by feeding the disc away from the edge along the same 45° radial line. The experimental results are also shown in a display of the real and imaginary parts of the input impedance as a function of frequency. The resistance and reactance are shown for the case of d = .3175 cm for four different values of b/a in Figures 3-6. Similar graphs for the case of d = .1575 cm are shown in Figures 7-10.

The deviation from a circle seen in Figure 2 is manifest in the double peaking behavior seen for the same antenna in Figure 5. The impedance of the radiators that are most nearly circular (Figures 3 and 7) are seen to resemble the impedance of a circular disc as one would expect. As the disc becomes more elliptical (Figures 4 and 8) two distinct resonances begin to appear. This feature is more apparent in the 0.1575 cm thickness case

since the resonance curve for the circular disc of this thickness is approximately half as wide as for the thicker case. Even though the resonance curves in Figures 3-10 are seen to be broader in the double resonance cases the polarization does not remain circular over this larger impedance bandwidth. At the first of the double peaks the radiation is linearly polarized along the major axis of the ellipse. As the frequency is increased the radiation becomes more nearly circularly polarized. As the second peak is approached the radiation becomes linearly polarized again, but this time oriented along the minor axis of the ellipse.

III. Radiation Patterns

To investigate the polarization of the radiated fields from these elliptical printed-circuit antennas, far field radiation patterns were measured. Since the possibility of circular polarization was of concern, all patterns were taken with a spinning, linear-polarized horn. The printed-circuit antenna itself was used as the source by attaching a small, lightweight, battery-powered transmitter directly to the back of the ground plane of the antenna. This transmitter assembly was placed on the rotating table inside an anechoic chamber and the spinning horn then used as the receiver.

Radiation patterns are shown in Figures 11-13 for three different ratios of b/a with the same thickness d = .3175 cm. The $\phi = 90°$ plane represents a cut directly over the minor axis of the ellipse. Similar patterns were also recorded for cuts made over the major axis and over the feed point of the disc. The frequencies were chosen by experimentally finding the frequency for which the axial ratio was a minimum at $\theta = 0°$ (normal to the plane of the disc).

For each case the spin-linear measured patterns are shown by the solid line. In addition the theoretical maximum and minimum fields for all possible orientations of the linear polarized receiving antenna are shown for this frequency and geometry. The curve is normalized only at the point of the maximum field at $\theta = 0$. It is seen that both the theoretical curves and the experimental data confirm that for a properly chosen eccentricity and frequency the resulting radiation is quite nearly circularly polarized (about 1 dB for b/a = .976 in Figure 12). This circularity is seen to deteriorate both for the case when the disc is made more circular (Figure 11) and when it is made more elliptical (Figure 13).

To investigate its dependence on frequency the axial ratio at $\theta = 0°$ was measured for each antenna as the frequency was varied. Using the exact dimensions of the experimental antennas and the manufacturer's stated value of dielectric constant ($\epsilon_r = 2.48$) the theoretical curves accurately indicate the lowest value of axial ratio and the general shape of the curves for each eccentricity. However, the frequency for which the minimum axial ratio occurs is not well predicted. For this reason a search for the indicated value of dielectric constant was made using the theoretical formulas and the experimentally found frequency of minimum axial ratio. For each different antenna, the best value was found to be $\epsilon_r = 2.41$. Thus in Figure 14, the experimental data and the theoretical curves for this value of dielectric constant are shown. Reasonable correlation is seen for all aspects of the theory and experiment. (Use of $\epsilon_r = 2.48$ would simply shift the theoretical curves to the right along the frequency axis.)

These curves indeed show that there exists an optimum eccentricity and also give an indication of possible frequency bandwidth. As noted earlier,

this bandwidth due to polarization is even narrower than the impedance band-
width measured in the previous section. Even for the best antenna
(b/a = .976), the axial ratio is less than 6 dB only over the range from
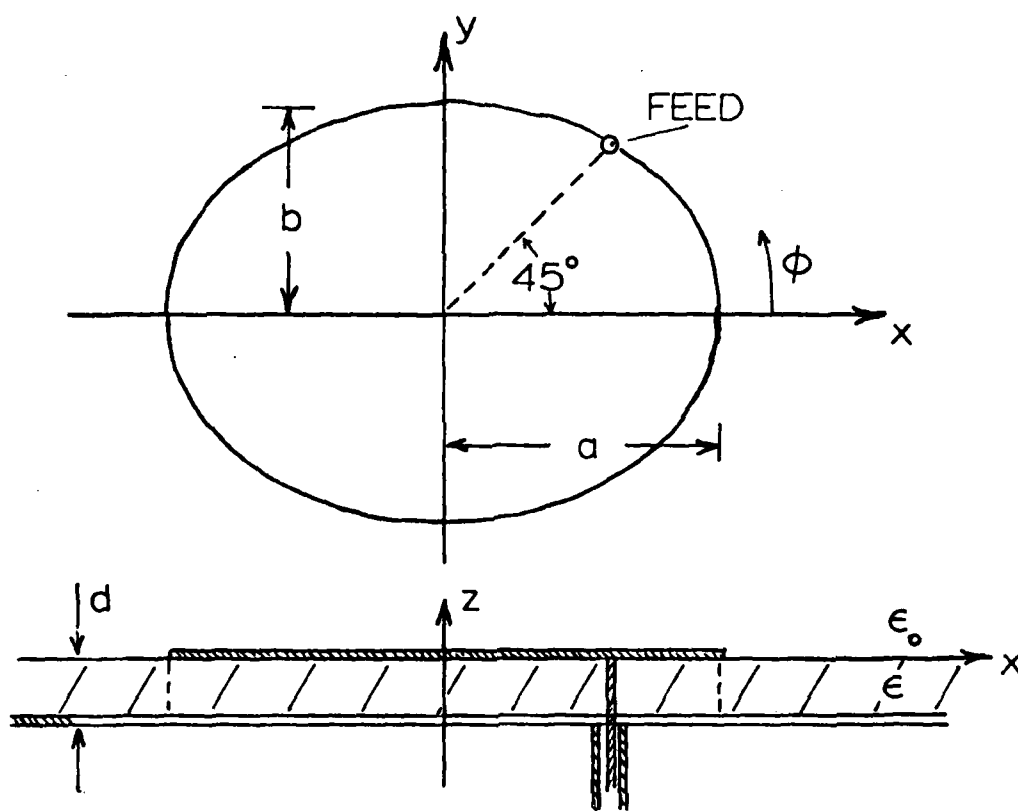1.33 to 1.35 GHz or a bandwidth of 1.5%.

IV. Conclusions

It has been shown that with the proper choice of eccentricity and fre-
quency the elliptical printed-circuit antenna can provide a circularly
polarized radiation field using only a simple single feed network. The
behavior of its impedance, pattern and axial ratio as a function of eccen-
tricity, frequency, and dielectric thickness has also been investigated.
It is seemingly an excellent design choice when both the usual character-
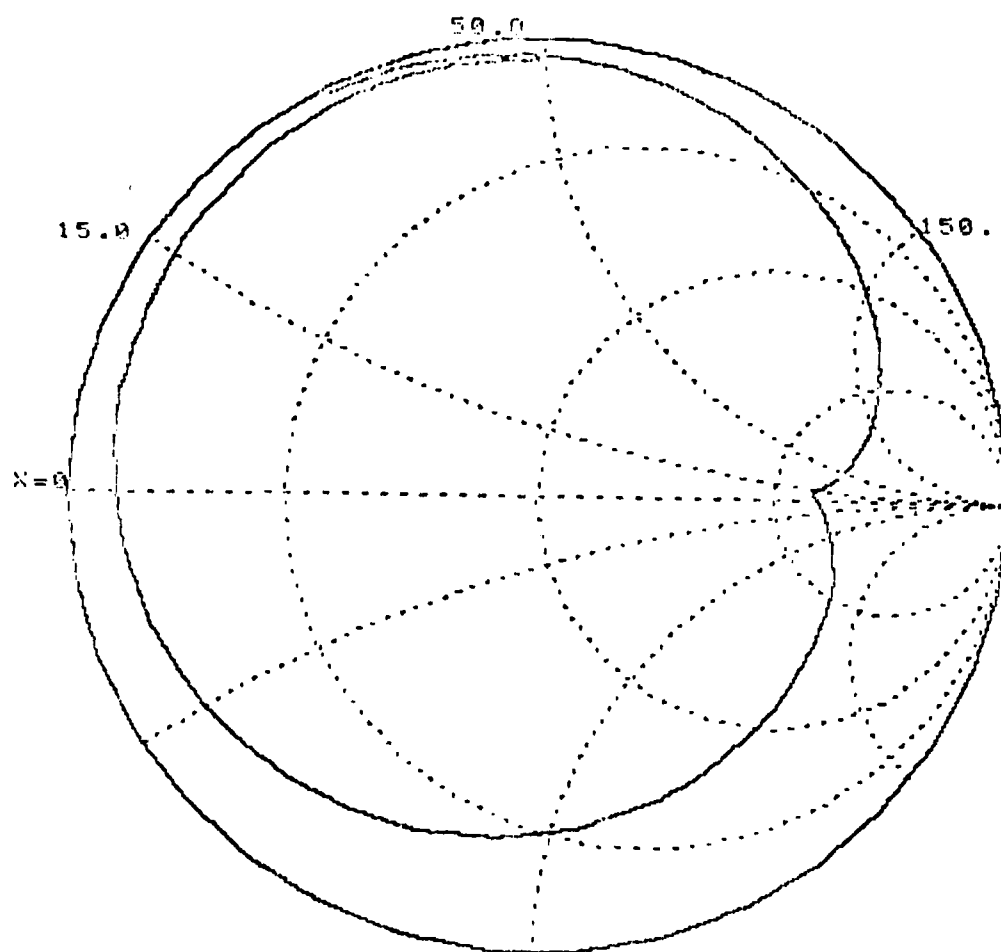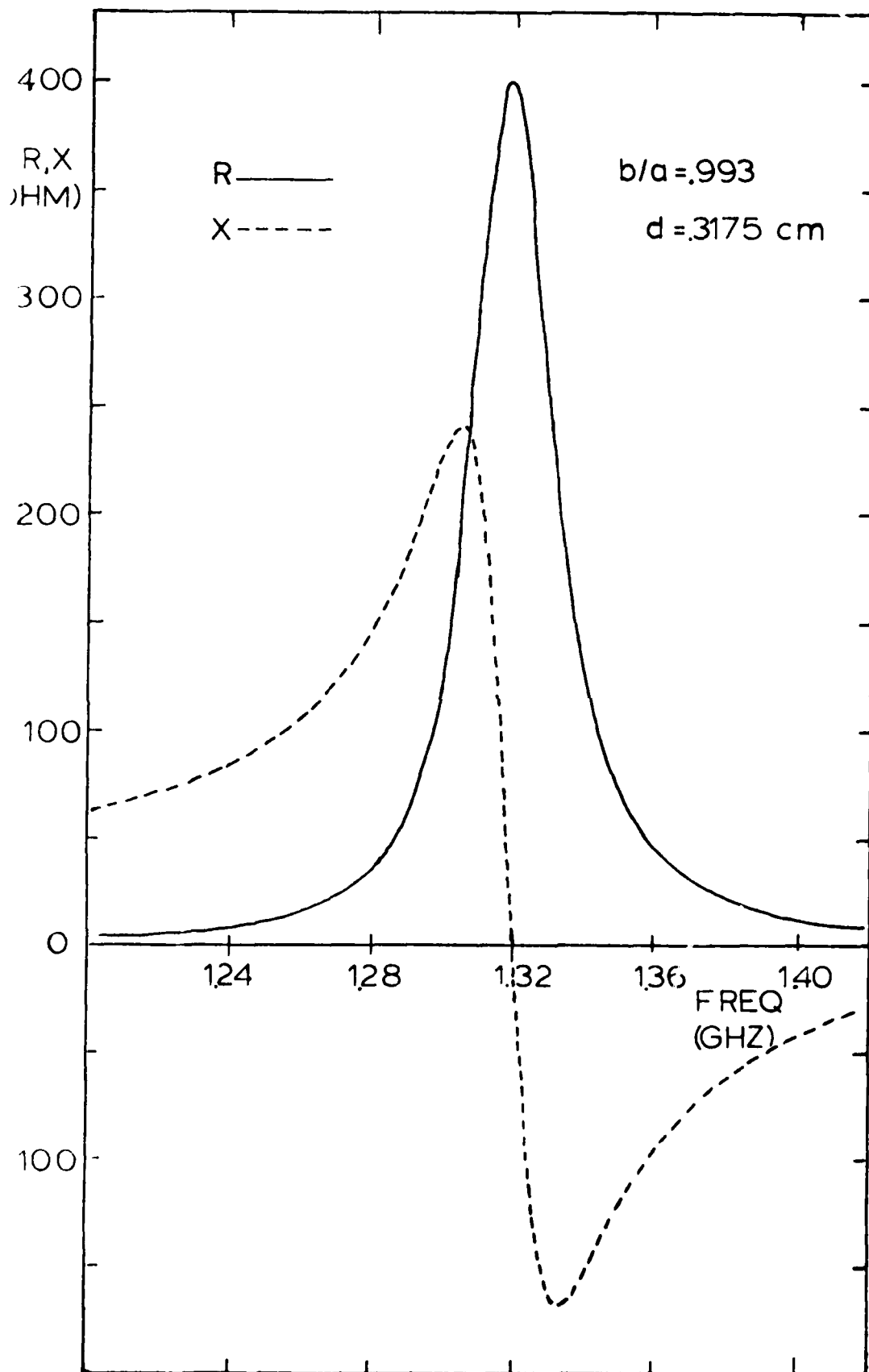istics of printed-circuit antennas and circular polarization are required.

References

[1] H. D. Weinschel, "A cylindrical array of circularly polarized micro-
    strip antennas", IEEE AP-S International Symposium Digest, pp. 175-180,
    June 1975.

[2] W. F. Richards, Y. T. Lo, and P. Simon, "Design and theory of circu-
    larly polarized microstrip antennas," 1979 IEEE AP-S International
    Symposium Digest, pp. 117-120.

[3] J. L. Kerr, "Microstrip polarization techniques", Proceedings of the
    Antenna Applications Symposium, University of Illinois, 1978.

[4] L. C. Shen, "The elliptical microstrip antenna with circular polariza-
    tion", submitted to IEEE Trans. Antennas and Propagation.

[5] I. P. Yu, "Low profile circularly polarized antenna", NASA Report
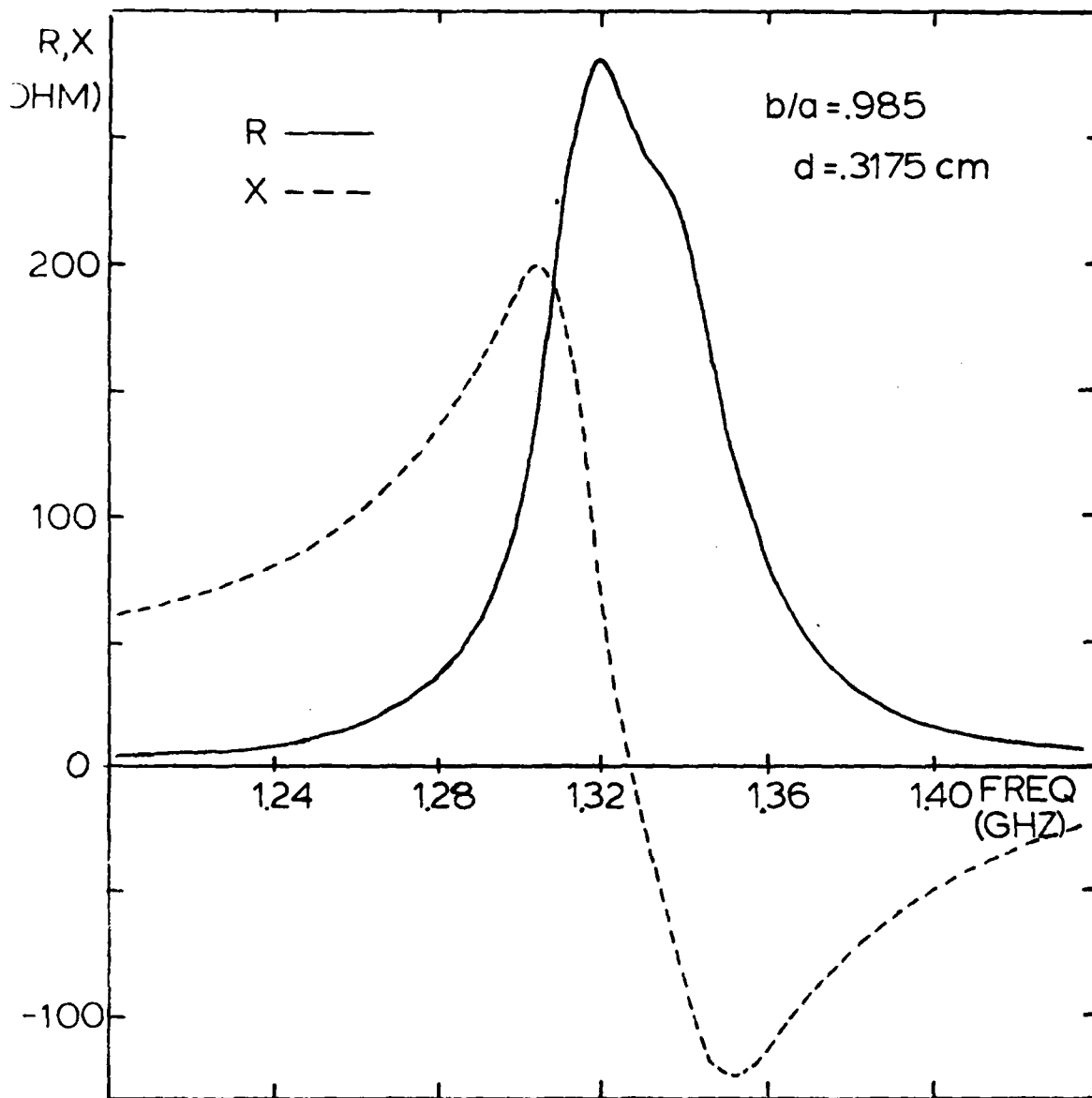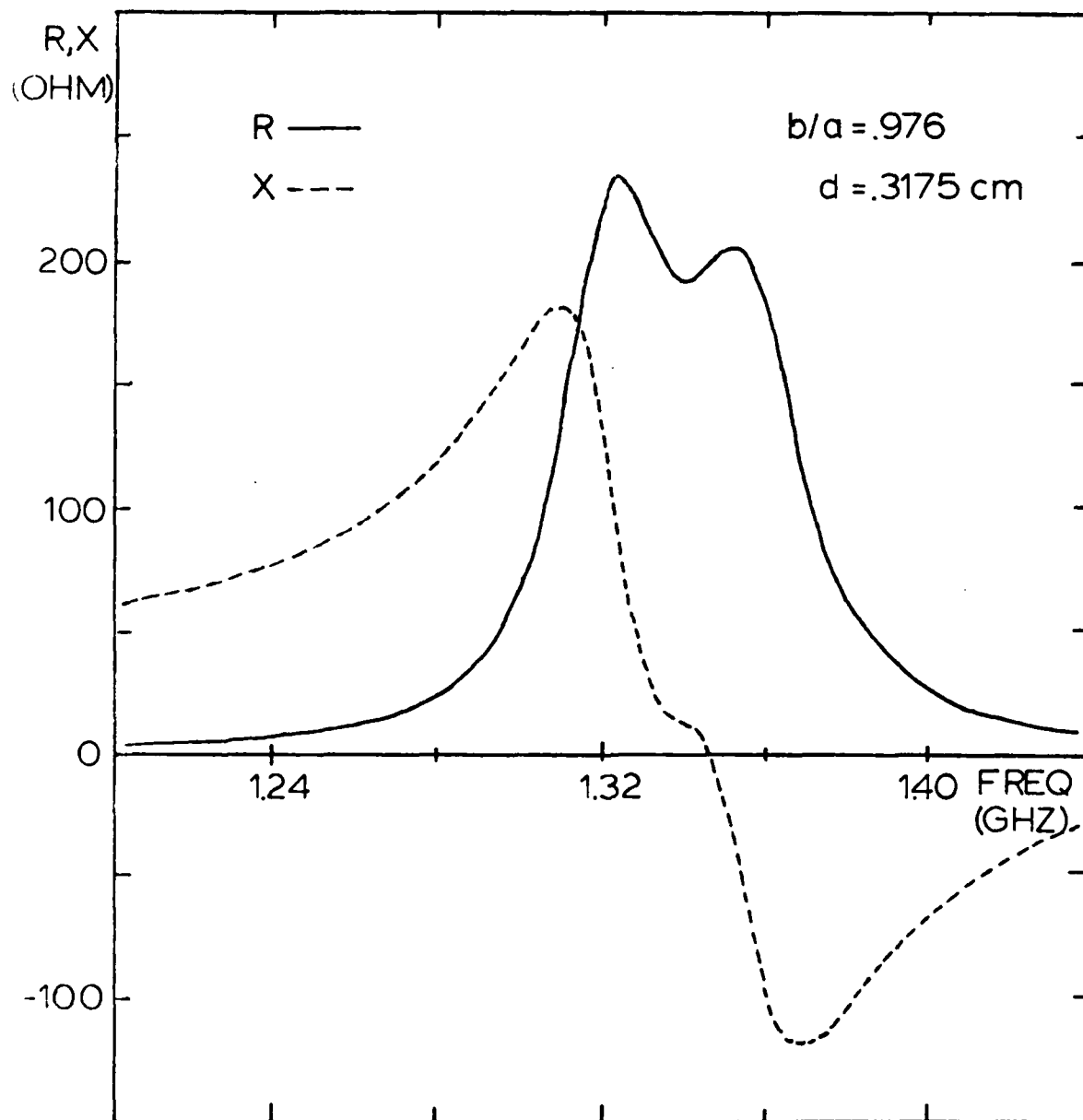   N78-15332, 1978.

List of Captions

Figure 1.   Geometry of elliptical printed-circuit antenna

Figure 2.   Smith chart display of impedance (d = .3175 cm; b/a = .976)

Figure 3.   Impedance versus frequency (d = .3175 cm; b/a = .993)

Figure 4.   Impedance versus frequency (d = .3175 cm; b/a = .985)

Figure 5.   Impedance versus frequency (d = .3175 cm; b/a = .976)

Figure 6.   Impedance versus frequency (d = .3175 cm; b/a = .960)

Figure 7.   Impedance versus frequency (d = .1575 cm; b/a = .996)

Figure 8.   Impedance versus frequency (d = .1575 cm; b/a = .983)

Figure 9.   Impedance versus frequency (d = .1575 cm; b/a = .976)

Figure 10.   Impedance versus frequency (d = .1575 cm; b/a = .962)

Figure 11.   Radiation pattern (d = .3175 cm; b/a = .985)

Figure 12.   Radiation pattern (d = .3175 cm; b/a = .976)

Figure 13.   Radiation pattern (d = .3175 cm; b/a = .960)

Figure 14.   Axial ratio versus frequency (d = .3175 cm)

θ=30
F =1330 MHZ
d=.3175 cm
b/a=.985
φ=90°

60°

θ=30°
--- THEORY
— EXP.

10 DB

20

30

60°

0   10   20   30   30   20   10   0

θ=30°

F=1339 MHZ
b/a=.976
d=3175 cm
φ=90°

60°

θ=30°
--- THEORY
—— EXP.

10 DB

20

30

60°

0   10   20   30   30   20   10   0

θ=30°   θ=30°

F=1342 MHZ
d=.3175 cm
b/a =.960
φ=90°

10 DB

60

20

30

----THEORY
—— EXP.

0   10   20   30   30   20   10   0